Momentum Budget of a Squall Line with Trailing Stratiform Precipitation: Calculations with a High-Resolution Numerical Model

MING-JEN YANG* AND ROBERT A. HOUZE JR.

Department of Atmospheric Sciences, University of Washington, Seattle, Washington

(Manuscript received 3 July 1995, in final form 20 June 1996)

ABSTRACT

In this paper, the authors investigate the momentum budget of a squall line with trailing stratiform precipitation by examining how the momentum balance varies with respect to the storm's internal structure. In particular, the authors determine differences between the momentum budgets of the convective and stratiform precipitation regions, which are physically distinct parts of the storm. The results from a high-resolution nonhydrostatic numerical simulation of the two-dimensional segment of the 10–11 June 1985 PRE-STORM squall line are used. The momentum equation is averaged over a 300-km-wide large-scale area for time periods of 1 h. On the 1-h timescale, the convective-scale temporal variations of horizontal and vertical velocities are nearly uncorrelated, and thus their contribution to the momentum flux is negligible. The remaining standing-eddy and mean-flow circulations account for the momentum flux on this timescale. The combination of the standing eddy and mean flow behave almost exactly like Moncrieff's idealization of two-dimensional steady-state squall line flow.

Because the standing-eddy circulation and the pressure-gradient acceleration vary from one part of the storm to another, the interplay of forces leading to the large-scale momentum tendency also differs strongly from one subregion to another. The convective precipitation region dominates the momentum budget at low levels, where the standing-eddy flux convergence produces a forward acceleration that slightly outweighs the rearward pressure-gradient acceleration. At midlevels, both the convective and stratiform precipitation regions contribute to the net large-scale momentum tendency. The pressure-gradient forces in the convective and stratiform precipitation regions are both strong but oppositely directed; however, the rearward standing-eddy flux convergence in the convective precipitation region is also strong; thus, the net large-scale momentum tendency at midlevels is rearward. At upper levels, the momentum budget is completely dominated by the stratiform precipitation region, where a strong forward-directed pressure-gradient acceleration dominates the net large-scale momentum tendency.

These differences between the momentum budgets of the convective and stratiform precipitation regions suggest that rather different large-scale momentum tendencies can arise as a function of storm structure; storms with strong convective precipitation regions and weak stratiform precipitation regions would produce momentum tendencies quite different from storms with well-developed stratiform precipitation regions.

1. Introduction

Schneider and Lindzen (1976) and Stevens et al. (1977) pointed out the importance of vertical momentum transport by deep convection in large-scale dynamics. For many convective clouds, convective momentum transport may be downgradient, reducing the wind shear of mean flow as predicted by the mixing-length theory. However, Moncrieff (1981) showed that organized deep convective systems (like squall lines) could transport momentum in a countergradient sense, increasing the wind shear of large-scale mean flow. This countergradient momentum transport associated with organized deep convection must be accounted for in cumulus parameterization schemes in mesoscale and large-scale numerical models.

Observations of tropical squall lines show that the vertical flux of horizontal momentum can be countergradient in the cross-line direction and downgradient in the along-line direction (LeMone 1983; LeMone et al. 1984). Gao et al. (1990) obtained a similar result in a mesoscale model (MM4) simulation of the 10–11 June 1985 squall line in the Preliminary Regional Experiment for Stormscale Operational Research Meteorology (PRE-STORM) (Cunning 1986). They investigated the meso-β-scale[1] momentum budget and its effects on large-scale mean flow, and found that cross-line momentum generation was the strongest contributor to the momentum budget. Convectively generated downdrafts were as important as updrafts in vertically

Corresponding author address: Dr. Ming-Jen Yang, Dept. of Atmospheric Sciences, University of Washington, Box 351640, Seattle, WA 98195-1640.
E-mail: mingjen@atmos.washington.edu

[1] Meso-β-scale is defined by Orlanski (1975) as a horizontal dimension of 20–200 km.

transporting horizontal momentum within both the convective and stratiform regions.

Gallus and Johnson (1992) used rawinsonde data to diagnose the momentum fluxes and tendencies in the 10–11 June 1985 squall line observed in PRE-STORM. They found a strong midlevel mesolow, which contributed to the rear-to-front (RTF) tendency in the vicinity of a rear inflow jet. This mesolow also led to a strong front-to-rear (FTR) tendency elsewhere through most of the storm. The vertical flux of cross-line momentum in the convective precipitation region during the mature and dissipating stages was countergradient below 500 mb, in agreement with previous studies of LeMone et al. (1984) and Gao et al. (1990). However, the rawinsonde data they used did not fully resolve the leading convective precipitation region.

LeMone and Moncrieff (1994) investigated the effects of quasi-two-dimensional convective bands on the environmental flow by comparing observed mass fluxes, momentum fluxes, and horizontal pressure changes to those predicted by the idealized dynamical model of Moncrieff (1992). Despite assumptions of two-dimensionality, steady state, and no Coriolis or buoyancy effects, they showed that Moncrieff's (1992) model successfully predicted both the amplitude and shape of vertical mass and momentum fluxes for mesoscale convective systems (MCSs) in near-neutral environments (low buoyancy or high shear) and with system width-to-depth ratios close to the value of 4:1. However, the model was less successful for systems in more unstable environments or those with large horizontal extent, probably because of the neglect of the generation of horizontal momentum by buoyancy.

The quasi-two-dimensional squall line prototype idealized by Moncrieff (1992) describes well the overall dynamics of squall lines with leading-line/trailing-stratiform structure; however, it leaves unaddressed certain details of the microphysical–dynamical interactions. In such cases, a rapidly moving line of intense convective cells is followed by a region of stratiform precipitation. The convective and stratiform precipitation regions are distinct both kinematically (Houze 1982, 1989) and microphysically (Houze 1989, 1993; Braun and Houze 1994a,b, 1995a,b), and the large-scale flow responds fundamentally differently to the vertical heating profiles in these two regions (Mapes 1993; Mapes and Houze 1995). The radar echo structure in the convective and stratiform precipitation regions is also distinct, as a result of the different kinematics and microphysics, and techniques are available to separate the convective and stratiform precipitation regions based on their different reflectivity structure (Churchill and Houze 1984; Steiner et al. 1995).

Until now, the separate roles of the convective and stratiform precipitation regions have not been investigated in terms of how they may influence the large-scale horizontal momentum field. The objective of this study is thus to investigate the momentum budget of a two-dimensional squall line with leading-line/trailing-stratiform structure and thereby gain insight into the contributions of the convective and stratiform precipitation regions to the momentum transports over a large-scale region containing the storm.

To achieve this objective, we make use of the numerical simulation results of Yang and Houze (1995a,b). Their simulation is for the 10–11 June 1985 squall line in PRE-STORM (Augustine and Zipser 1987; Smull and Houze 1987; Johnson and Hamilton 1988; Rutledge et al. 1988; Zhang et al. 1989; Zhang and Gao 1989; Gallus and Johnson 1991, 1992; Biggerstaff and Houze 1991a,b, 1993; Braun and Houze 1994a,b, 1995a,b). The two-dimensional portion of the storm was identified by Biggerstaff and Houze (1993), who constructed a composite analysis of the Doppler radar data in a 60-km-wide strip across the north-central portion of the storm where both the reflectivity and horizontal flow patterns appeared to be the most nearly two-dimensional. Yang and Houze (1995a) verified their model calculations by comparing the analyses of Biggerstaff and Houze (1993) and showed that the model describes reasonably well the portion of the squall line that exhibited the highest degree of two-dimensionality. To the north and south of the quasi-two-dimensional region of the storm, the squall line displayed strongly three-dimensional circulations, which require three-dimensional models and consideration of Coriolis effects (Zhang et al. 1989; Zhang and Gao 1989; Skamarock et al. 1994). In the present study, we do not pursue these broader three-dimensional features. Rather, we extend the study of the two-dimensional aspects of squall systems by examining the momentum budget and transports of the two-dimensional region.

2. Model description

The numerical model used in this study is a two-dimensional (2D) version of the Klemp and Wilhelmson (1978) compressible nonhydrostatic cloud model, as modified by Wilhelmson and Chen (1982; see Yang and Houze 1995a,b for model details). The x direction parallels the propagation of the squall line. There is no along-line variation of any variable, and there is no along-line velocity component. The basic-state environment is assumed constant in time and horizontally homogeneous. Coriolis force, surface drag, and radiation effects are neglected. The grid is stretched both vertically and horizontally. The grid size (Δz) of the lowest layer is 140 m; the grid size of the highest layer is 550 m; and the model top is at 21.7 km. Following Fovell and Ogura (1988), the model has a 314-km-wide fine mesh with 1-km resolution in the center of the domain; there are 70 grid points in the horizontally stretched grids located on both sides of the fine mesh; the ratio between adjacent grid spacings is 1.075:1. The total horizontal domain size (fine mesh and horizon-

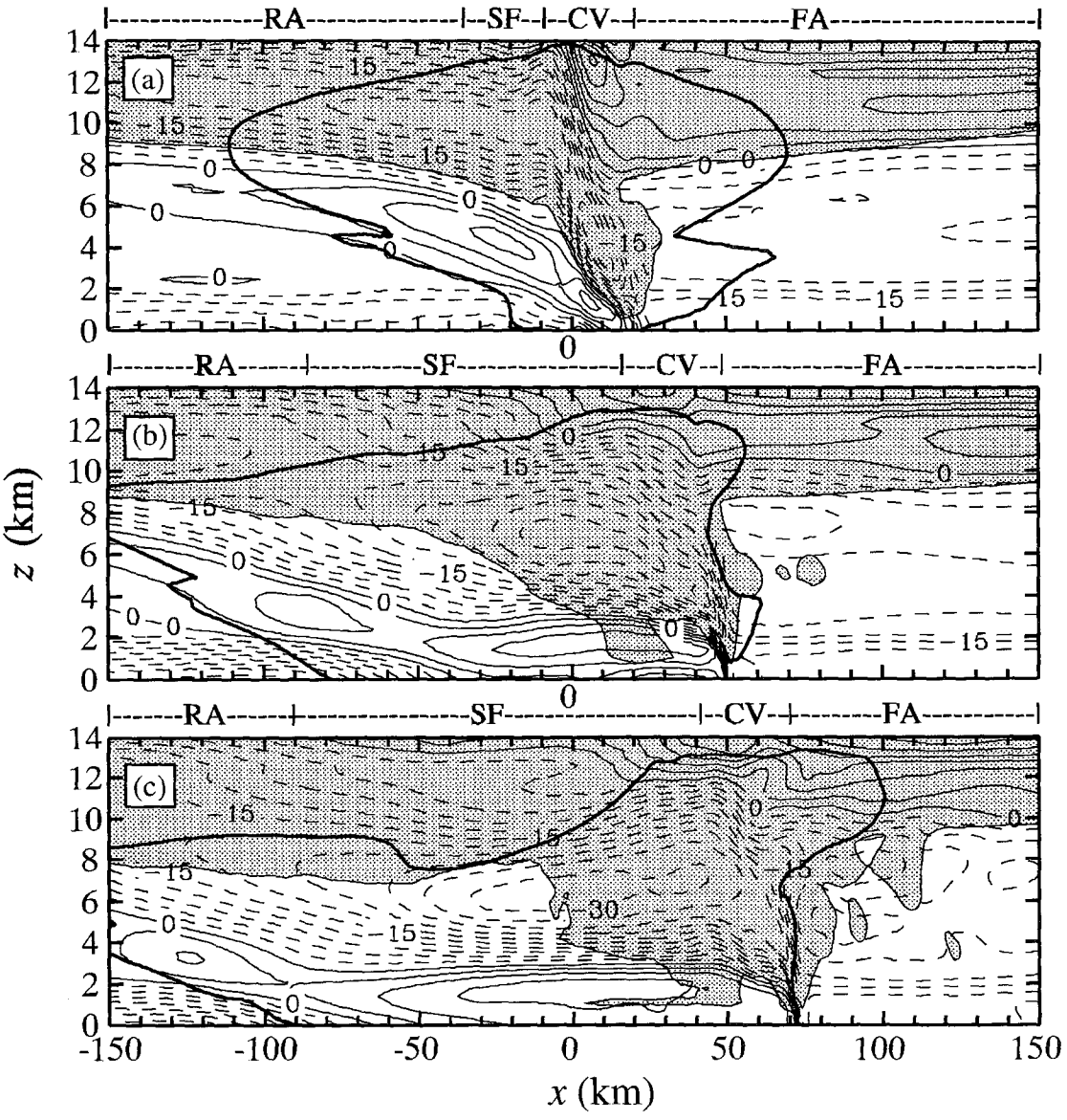

FIG. 1. Storm-relative horizontal wind ($u - c$; contour interval is 3 m s^{-1}) averaged during (a) the initial stage (t = 7.5–8.5 h), (b) mature stage (t = 10–11 h), and (c) the slowly decaying stage (t = 12.5–13.5 h) of the simulated storm. RTF flow is shown in solid lines, and FTR flow is dashed. Shaded cloudy region is determined by the time-averaged nonprecipitating hydrometeor (cloud water and cloud ice) mixing ratio greater than 0.1 g kg^{-1}. Heavy outline is the storm precipitation boundary determined by the time-averaged modeled radar reflectivity of 15-dBZ contour. Regions of CV, SF, RA, and FA are shown in the bars above. (From Yang and Houze 1995b.)

tally stretched grids combined) is 4814 km. The model domain translates with the storm such that the simulated storm is always within the fine mesh.

Yang and Houze (1995a) showed that the model simulates the mature stage kinematic fields reasonably well in comparison with those determined from the dual Doppler radar analysis of Biggerstaff and Houze (1993). Yang and Houze (1995a) also performed a three-dimensional simulation, which showed that the basic cross-line features of the squall-line convective system analyzed in this study are properly represented in the 2D framework. The initial environmental conditions are based on the 2331 UTC 10 June 1985 sounding obtained at Enid, Oklahoma, 4 h before the squall line passed this station (see Fig. 3 of Yang and Houze 1995a). Convection was triggered by a 5-km deep, 170-km wide cold pool with a 6-K potential temperature deficit and a 4 g kg^{-1} water vapor deficit (see Fig. 5 of Yang and Houze 1995a). The model was integrated for 15 h. Another triggering mechanism (a warm

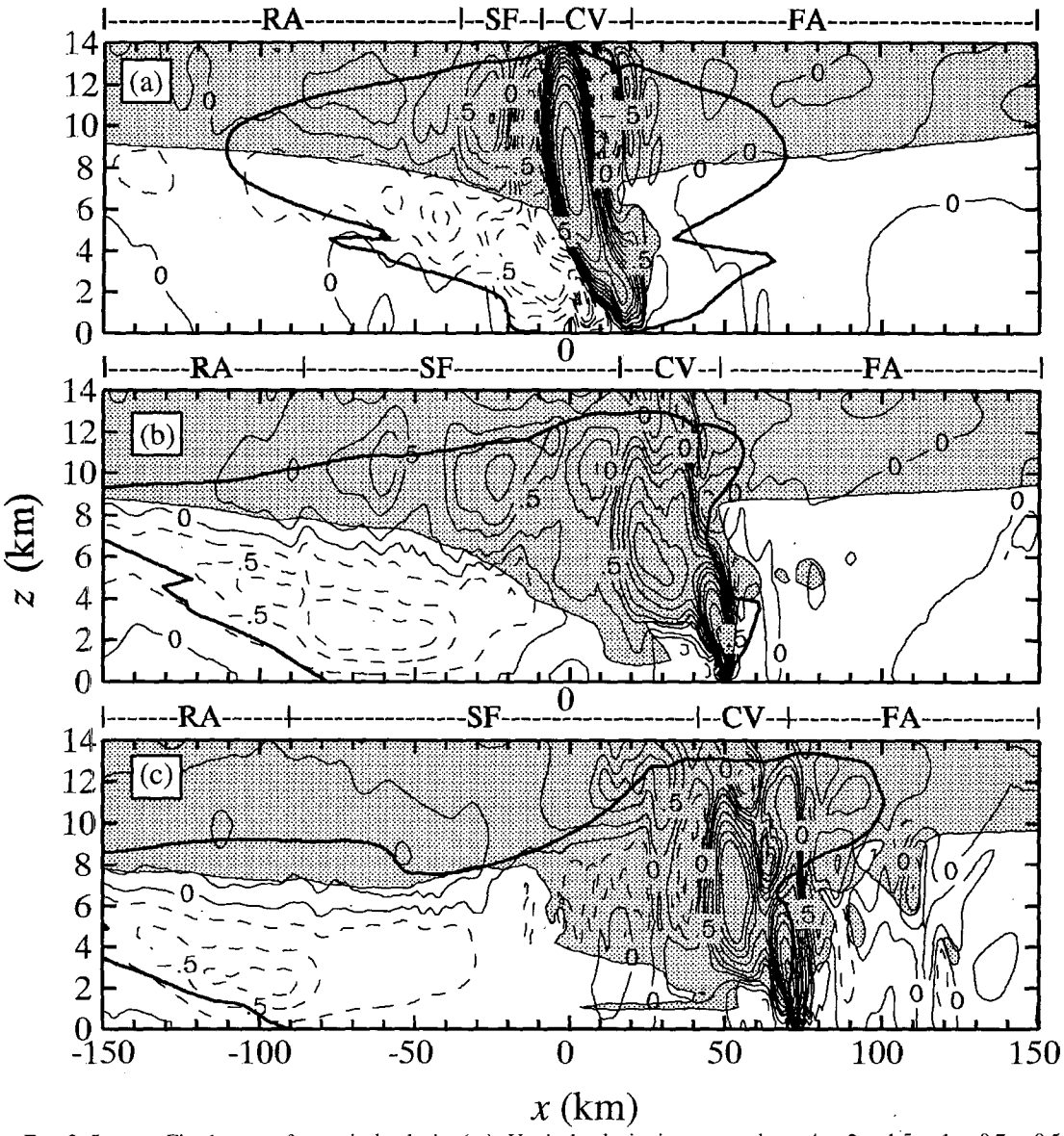

FIG. 2. Same as Fig. 1 except for vertical velocity (w). Vertical velocity is contoured at −4, −2, −1.5, −1, −0.7, −0.5, −0.2, 0, 0.2, 0.5, 0.7, 1, 1.5, 2, 2.5, 3, 4, 5, 7, 10, and 13 m s^{-1}. Positive field is in solid lines, and negative field is dashed. (From Yang and Houze 1995b.)

bubble) and a cold pool with different strength (8 and 10 K) are also used to initiate the convection. Once the simulated storms reach their mature stage, they all show similar kinematic and thermodynamic structures, consistent with Fovell and Ogura (1988). Therefore, the delicate momentum balance within the storm is not sensitive to the initial arbitrary trigger.

3. Simulation results

a. Stages of storm development

Figures 1–4 show kinematic, thermal, and pressure fields for three 1-h periods during the lifetime of the storm. The three time periods (t = 7.5–8.5 h, 10–11 h, and 12.5–13.5 h) represent the initial, mature, and slowly decaying stages of storm development. The figures are in a coordinate frame moving at the speed of the storm's gust front: 9.4, 12.2, and 12.0 m s^{-1} in the initial, mature, and late stages, respectively. Note that the 1-h time averaging is taken in the storm-relative framework where the leading edge of the storm is at a fixed point during three 1-h periods. Because of the assumed constant convectively favorable condition in the prestorm environment, the simulated storm did not actually die before the end of simulation (t = 15 h); however, after the

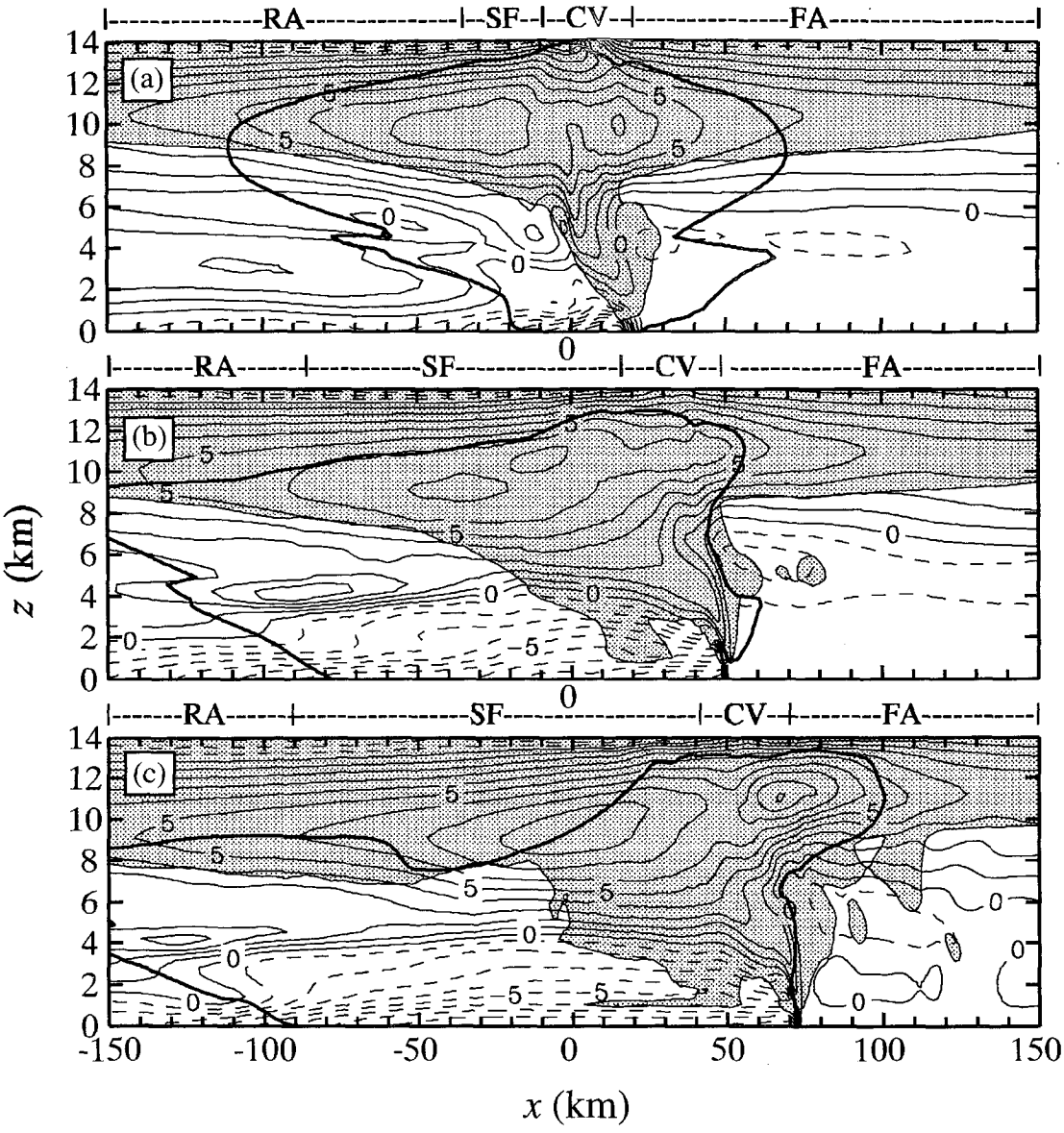

FIG. 3. Same as Fig. 1 except for potential temperature perturbation (θ'; contour interval is 1 K). Positive field is in solid lines, and negative field is dashed. (From Yang and Houze 1995b.)

mature stage (t = 10–11 h), the simulated storm did show a slowly weakening trend.

Regions of convective precipitation (CV), stratiform precipitation (SF), rear anvil (RA), and forward anvil (FA) are indicated in the bar above each panel in Figs. 1–4. The partition between the convective and stratiform precipitation regions is based on simulated surface rainfall rate [see Fig. 4 of Yang and Houze (1995b) for the rainfall-rate distribution of the simulated squall line]. The *convective precipitation region* either has a surface rainfall rate greater than or equal to 15 mm h^{-1}, or the gradient of rainfall rate is greater than 5 mm h^{-1} km^{-1}. The surface precipitation region not satisfying these criteria is defined as the *stratiform precipitation region.* These criteria are consistent with the convective–stratiform separation methods applied to radar data by Churchill and Houze (1984) and Steiner et al. (1995).

b. Kinematic fields

The storm-relative horizontal wind field consisted of several distinct layers. Initially, there was a strong inflow from the boundary layer ahead of the storm and a mid-to upper-level ascending FTR flow in the interior of the storm (Fig. 1a). Below the ascending FTR flow

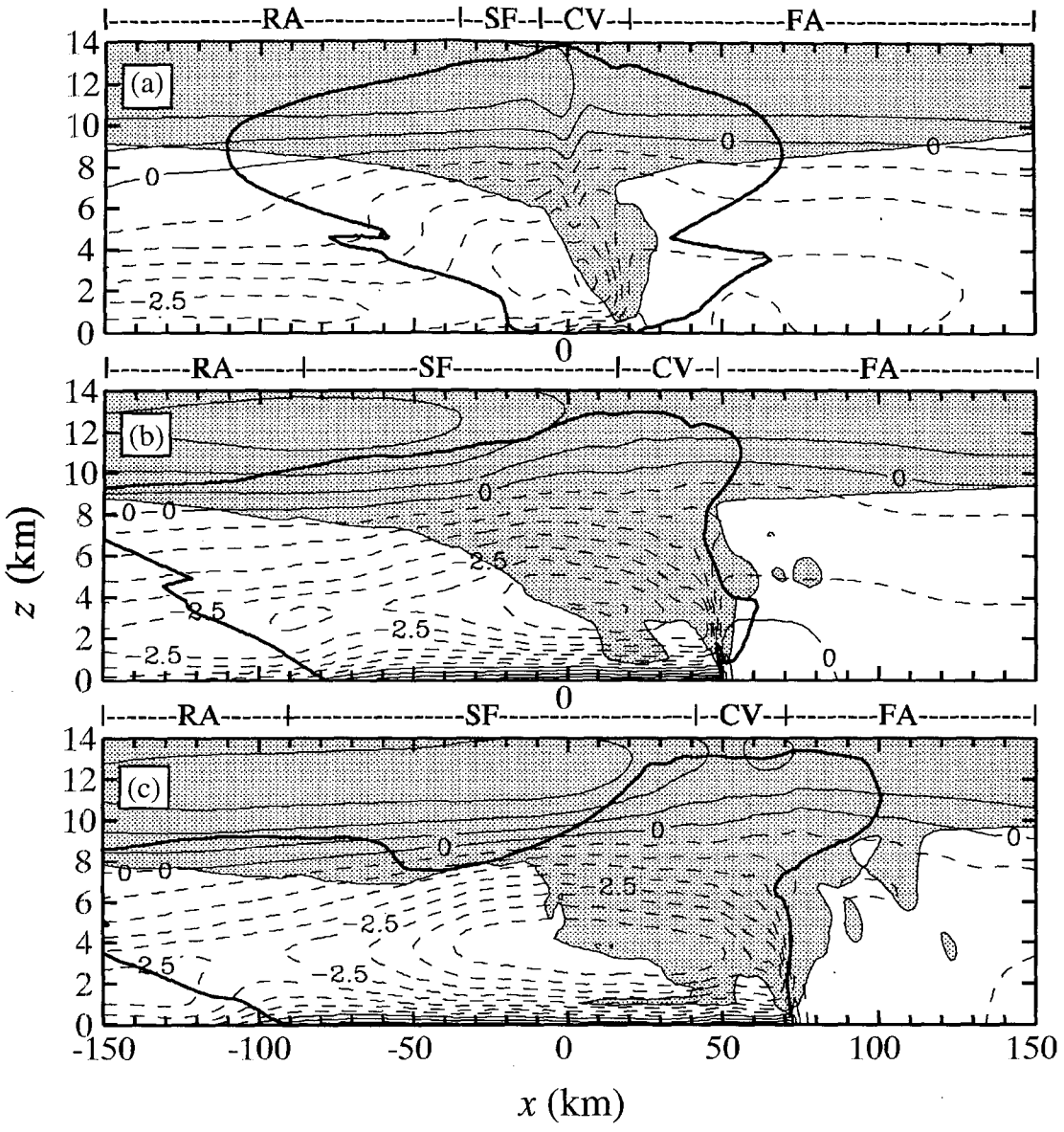

FIG. 4. Same as Fig. 1 except for pressure perturbation (p'; contour interval is 0.5 mb). Positive field is in solid lines, and negative field is dashed. (From Yang and Houze 1995b.)

was a low- to midlevel descending RTF flow. Underneath the midlevel RTF flow was a low-level FTR flow. As the storm matured (Fig. 1b), the ascending FTR flow became stronger, broader, and more horizontal; the descending RTF flow also became more organized and exhibited a pronounced double-core structure during the mature stage. By the late stage (Fig. 1c), both the ascending FTR flow and descending RTF flow were more horizontal. It was discussed in Yang and Houze (1995b) that, because of the neglect of background baroclinicity and/or the enhanced mass convergence associated with vortices on both ends of a fully 3D squall line, the rear inflow at the back edge of the simulated 2D storm only reaches half of the observed strength (8 m s^{-1} vs 15 m s^{-1}) at the mature stage.

The vertical air motions initially consisted of intense deep updrafts at the leading edge of the storm (Fig. 2a). Strong downdrafts surrounded the updrafts at upper levels, as a result of mass compensation (Houze 1993, 223–226). Vertical motions were generally weak in the stratiform precipitation region ($x = -30$ to 0 km).

As the storm matured, there were two main updrafts in the convective precipitation region ($x = 20$–50 km in Fig. 2b). At the leading edge, a low-level updraft was persistently forced by the strong con-

vergence near the gust front. About 20 km behind the gust front, a midlevel updraft was a free convective updraft associated with the release of latent heat of condensation. In the trailing-stratiform precipitation region, weaker ascent occurred at upper levels above a region of weak descent. These regions of upper-level ascent and lower-level descent in the stratiform precipitation region are often referred to as the *mesoscale updraft* and *mesoscale downdraft* in this type of storm (e.g., Houze 1989). The mesoscale downdraft (the broad region of $w < -0.5$ m s^{-1} at $x = -120$ to -40 km in Fig. 2b) sloped downward toward the front of the storm, consistent with the dual-Doppler radar analysis (see Fig. 3d of Biggerstaff and Houze 1993). The mesoscale updraft (taken to be the broad region of $w > 0.5$ m s^{-1} at $x = -80$ to 0 km in Fig. 2b) was ahead of the mesoscale downdraft in the trailing-stratiform precipitation region, which was also found in the Doppler radar analysis. A weak mid- to upper-level downdraft (-0.3 to -0.2 m s^{-1}) was located in the transition zone (just behind the convective precipitation region; $x = 0-20$ km in Fig. 2b), although it does not show up clearly in the contour levels chosen for the figure. The transition zone downdraft was also seen in the radar data. By the late stage (Fig. 2c), mesoscale ascent and descent were weaker in the expanding stratiform precipitation region. The mid- to upper-level downdraft in the transition zone ($x = 30-45$ km in Fig. 2c), however, was stronger (-0.5 to -0.2 m s^{-1}).

c. *Thermal and pressure fields*

In the early stages of the storm, the potential temperature perturbation field (deviation from its initial value) indicated a warm plume of air produced in mid- to upper levels by the release of latent heat within the storm (Fig. 3a). This warm anomaly extended across the stratiform and rear anvil region. A second warm anomaly occurred below the rear anvil cloud at about 3-km altitude, as a result of an adiabatic temperature increase in the unsaturated descent of the mesoscale downdraft air (Zipser 1977; Johnson and Hamilton 1988). A low-level cold pool was produced by latent cooling of evaporation and melting associated with precipitation.

As the system matured (Fig. 3b), the thermal anomalies seen earlier broadened and intensified. The cold pool head was wider, deeper, and stronger (minimum surface θ' reached -10 K). The adiabatic warming in the mesoscale downdraft had produced a stronger warm anomaly above the back edge of the cold pool head ($z = 4-5$ km, $x = -100$ to -70 km). By the late stage (Fig. 3c), the system had continued to broaden; however, the cold pool was weaker (minimum surface θ' was -9 K), in association with weaker convective activity in the slowly decaying stage.

The pressure perturbation field (deviation from its initial value) in Fig. 4a shows a meso-γ-scale[2] low in the convective precipitation region, just behind the convective updraft at $z = 3$ km. It was hydrostatically generated as a result of the slope of warm convective updrafts (LeMone 1983; Fovell and Ogura 1988; Braun and Houze 1994a). Near the surface, there was a dynamically generated high pressure at the gust front (Fovell and Ogura 1988; Szeto and Cho 1994). Note that although the details of meso-γ-scale structure are smoothed out as a result of a 1-h time average, the convective region mesolow in Fig. 4a is still a meso-γ-scale low pressure, because of its associated strong pressure gradient, its small horizontal scale, and its proximity to the convective updrafts at the leading edge.

The meso-γ-scale low pressure anomaly centered at $z \approx 3-4$ km, $x \approx 0-20$ km in each panel of Fig. 4 is an important feature for the momentum budget. This low broadens and intensifies as the system progresses from the early (Fig. 4a) to mature stage (Fig. 4b). This broadening and intensification of the low corresponds to the amount of anomalously warm air above the low that increases during this period (Figs. 3a,b). This low pressure center continues to broaden into the weakening stage of the storm (Fig. 4c). The horizontal pressure gradient associated with this small-scale low affects the momentum budget of the storm by accelerating air in the convective precipitation region rearward and air in the stratiform precipitation region forward.

The surface high pressure associated with the cold pool reached its maximum strength ($p' = 2.4$ mb) during the mature stage of the storm (Fig. 4b). The simulated gust-front high pressure is of similar depth (1–1.5 km) and strength (2.1–2.4 mb), as compared to that from the radar retrieval result (see Fig. 6 of Braun and Houze 1994a) with similar data resolution.

The stratiform precipitation region also had a broad zone of high pressure near storm top. The horizontal pressure gradient associated with this high had a strong effect on the storm's momentum budget at upper levels. The rear anvil also had a low pressure anomaly at $z \approx 3-4$ km, $x \approx -95$ to -75 km in Fig. 4b. This feature, produced by subsidence warming of the descending rear inflow (Johnson and Hamilton 1988), extended to the surface as a weak wake low. The simulated mesolow is peaked at a higher elevation (at $z \approx 3$ km) than the observed mesolow [near the surface; Johnson and Hamilton (1988)].

The pressure perturbation field in the late stage of the storm (Fig. 4c) was similar to that in the mature stage. The meso-γ-scale low pressure in the convective precipitation region remained strong; however, the gust-front high pressure weakened.

[2] Meso-γ-scale is defined by Orlanski (1975) as a horizontal dimension of 2–20 km.

d. Subregional contributions to the large-scale mean horizontal and vertical velocity fields

Consider a 300-km-wide large-scale area A containing the simulated squall line like the fine-mesh domain shown in Fig. 1. The large-scale area A can be decomposed into four subregions:

$$A = A_{CV} + A_{SF} + A_{RA} + A_{FA}, \quad (1)$$

where A_{CV}, A_{SF}, A_{RA}, and A_{FA} are areas covered by convective precipitation, stratiform precipitation, rear anvil, and forward anvil, respectively. Then the area average of a physical quantity I over the large-scale area A can be written as

$$[I] = \sigma_{CV}\langle I\rangle_{CV} + \sigma_{SF}\langle I\rangle_{SF} + \sigma_{RA}\langle I\rangle_{RA} + \sigma_{FA}\langle I\rangle_{FA}, \quad (2)$$

where $[I]$ is the average of I over the large-scale area A; σ_{CV}, σ_{SF}, σ_{RA}, and σ_{FA} are fractions of large-scale area A covered by regions of convective precipitation, stratiform precipitation, rear anvil, and forward anvil, respectively (indicated in Table 1); and $\langle I\rangle_{CV}$, $\langle I\rangle_{SF}$, $\langle I\rangle_{RA}$, and $\langle I\rangle_{FA}$ are the averages of I over the corresponding subregions.

Figure 5 shows the large-scale-averaged vertical velocity [$I = w$ in (2)], and the contributions of subregions [terms on the right of (2)] during the mature stage of the storm. The vertical velocity averaged over the convective precipitation region (CV curve) is positive at all levels with a maximum value near z = 4 km. The vertical velocity averaged over the stratiform precipitation region (SF curve) shows mean ascent (the mesoscale updraft) in the upper troposphere ($z > 5.5$ km) and mean descent (the mesoscale downdraft) in the lower troposphere ($z < 5.5$ km). The area-weighted vertical velocity in the rear anvil region (RA curve) has a mean downdraft peaked near z = 5 km, corresponding to the descending rear inflow, and weak upward motion above ($z > 7.5$ km). The area-weighted vertical velocity in the forward anvil region (FA curve) shows a weak updraft peaked near the top of the boundary layer (z = 1.5 km), favorable for the development of new convective cells ahead of the gust front.

The vertical velocity averaged over the large-scale area A (Total curve) shows a mean updraft. As noted by Houze (1982, 1989), the large-scale ascent peaks at a higher level than that in the convective precipitation region (CV curve), owing to the effect of the mesoscale updraft/downdraft in the stratiform precipitation region (SF curve).

Figure 6 shows the contributions to the large-scale-averaged storm-relative horizontal wind [$I = u - c$ in (2)] by the four storm subregions during the mature stage. The large-scale horizontal wind (Total curve) is mainly determined by the stratiform precipitation region (SF curve), which shows strong FTR flow at mid-levels and RTF flow at low levels, while the contributions from other regions are small.

4. Evolution of momentum generation and advective processes

a. Time-averaged momentum equation

The horizontal momentum equation in a coordinate system moving with the squall line can be written as

$$\underset{\text{TEN}}{\frac{\delta u_s}{\delta t}} = \frac{\partial u_s}{\partial t} + c\frac{\partial u_s}{\partial x} = \underset{\text{PGF}}{-c_p\theta_{v0}\frac{\partial \pi}{\partial x}} \underset{\text{HAD}}{- u_s\frac{\partial u_s}{\partial x}} \underset{\text{VAD}}{- w\frac{\partial u_s}{\partial z}} \underset{\text{TRB}}{+ D_u}, \quad (3)$$

where

$$u_s = u - c. \quad (4)$$

Here, u is the ground-relative horizontal wind; c is the storm propagation speed; u_s is the storm-relative horizontal wind; x and z are the horizontal and vertical coordinates, respectively; $\delta/\delta t$ is the local derivative (or tendency, TEN) in the moving coordinate system; w is the vertical velocity; c_p is the specific heat at constant pressure; θ_{v0} is the basic-state virtual potential temperature; π is the nondimensional pressure perturbation; and D_u is the subgrid-scale turbulent mixing. A detailed derivation of Eq. (3) is given in Klemp and Wilhelmson (1978). Terms on the right-hand side of (3) are the pressure-gradient force (PGF) per unit mass, horizontal advection (HAD), vertical advection (VAD), and subgrid-scale turbulence (TRB). Note that the Coriolis force is not included.

The time-averaged form of (3) is

$$\overline{\frac{\delta u_s}{\delta t}} = -c_p\theta_{v0}\overline{\frac{\partial \pi}{\partial x}} - \overline{u_s\frac{\partial u_s}{\partial x}} - \overline{w\frac{\partial u_s}{\partial z}} + \overline{D_u}, \quad (5)$$

where

$$\overline{(\ )} \equiv \frac{1}{T}\int_{T_1}^{T_2} (\ )\,dt \quad (6)$$

and $T\,(=T_1 - T_2)$ is some finite time period. We let T = 1 h, and we take averages over three stages of the storm's lifetime: the *initial* stage (T_1 = 7.5 h, T_2 = 8.5 h), *mature* stage (T_1 = 10 h, T_2 = 11 h), and *slowly decaying* stage (T_1 = 12.5 h, T_2 = 13.5 h). The time resolution of the model output used to calculate the 1-h averages in (5) is 2 min.

b. Initial stage

Figure 7 shows the spatial distribution of one-hour-averaged momentum tendency (TEN), (PGF), and to-

TABLE 1. Fractions of the 300-km wide large-scale area A in Fig. 1 covered by subregions in three lifecycle stages of the simulated squall line.

Stages	Convective precipitation	Stratiform precipitation	Rear anvil	Forward anvil
Initial	0.10	0.10	0.37	0.43
Mature	0.10	0.33	0.24	0.33
Decaying	0.10	0.43	0.20	0.27

tal advection (ADV = HAD + VAD) during the initial stage (t = 7.5–8.5 h). (TRB) is not shown in Fig. 7 since it is generally small, being significant only near the intense convective updrafts or the cloud top (see Fig. 10), where mixing associated with entrainment and/or detrainment may be important.

Initially, the storm is characterized by intense convective updrafts at the leading edge and a steep RTF flow penetrating into the low levels at the leading edge from behind (see Figs. 1a and 2a). The momentum tendency in the convective precipitation region (x = −10 to 20 km in Fig. 7a) appears to be a small residual between large terms (pressure-gradient force, horizontal advection, and vertical advection), as indicated by Gao et al. (1990). Behind the convective precipitation region (x < −10 km), the momentum tendency shows the increasing FTR flow within the ascending FTR flow, increasing RTF flow within the descending RTF flow, and increasing FTR flow again within the low-level FTR flow (Fig. 7a). That is, these features are all intensifying.

Figure 7b shows that the pressure-gradient force accounts for most of the increasing intensity and downward extension of the descending RTF flow. Note that two maximum RTF increases (28 m s^{-1} h^{-1} near x = −20 km, z = 4 km, and 54 m s^{-1} h^{-1} near x = 5 km, z = 3 km) in Fig. 7b are collocated with the two RTF wind maxima in Fig. 1a. This result is consistent with previous studies of the 10–11 June storm (Gao et al. 1990; Gallus and Johnson 1992) and it also agrees with the conclusion of Yang and Houze (1995b) that the descending rear inflow is in part a dynamical response to the latent cooling processes of the squall line system. The pressure-gradient force also accounts for the strong negative tendency within the ascending FTR flow. Note again that two peak FTR tendencies (−116 m s^{-1} h^{-1} near x = −4 km, z = 9 km, and −112 m s^{-1} h^{-1} near x = 15 km, z = 2 km) by the pressure-gradient force in Fig. 7b are also collocated with the two FTR wind maxima in Fig. 1a.

In the convective precipitation region, total advection opposes the momentum changes produced by pressure-gradient force (Fig. 7c). Behind the convective precipitation region (x < −10 km), total advection generally supports the rearward extension of the as-

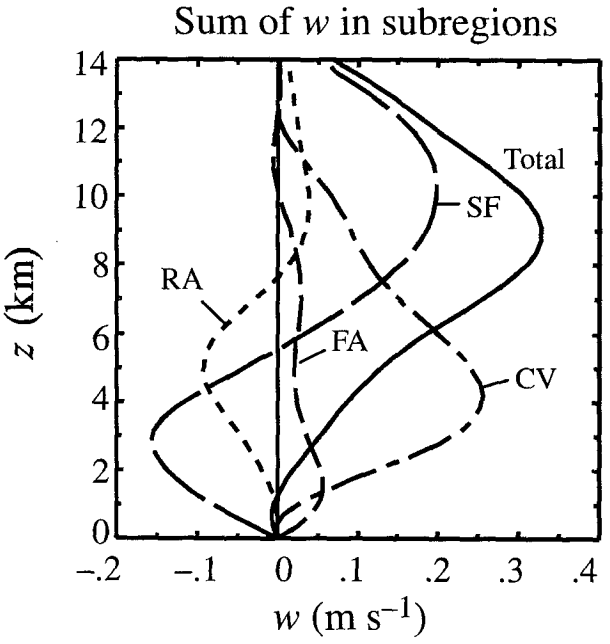

FIG. 5. Vertical velocity [I = w in (2)] averaged over the large-scale area A (Total curve) and its contributions by convective precipitation region (CV curve; $\sigma_{CV}\langle I\rangle_{CV}$), stratiform precipitation region (SF curve; $\sigma_{SF}\langle I\rangle_{SF}$), rear anvil region (RA curve; $\sigma_{RA}\langle I\rangle_{RA}$), and forward anvil region (FA curve; $\sigma_{FA}\langle I\rangle_{FA}$) during the mature stage (t = 10–11 h).

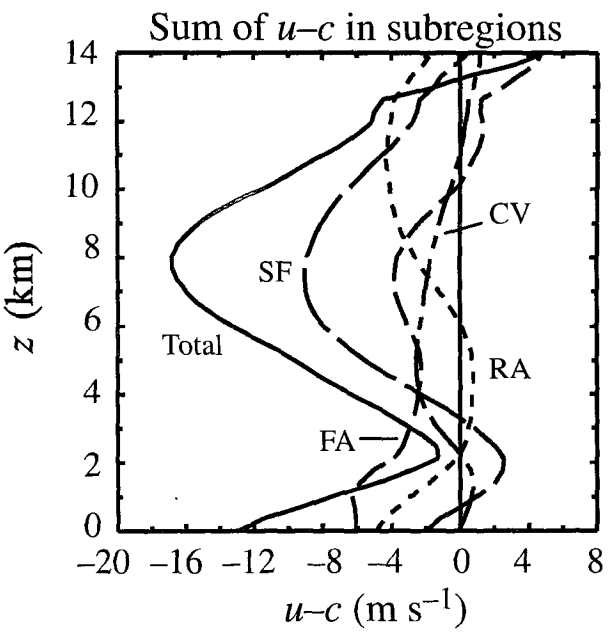

FIG. 6. Same as Fig. 5 except for the storm-relative horizontal wind [I = u − c in (2)] during the mature stage (t = 10–11 h).

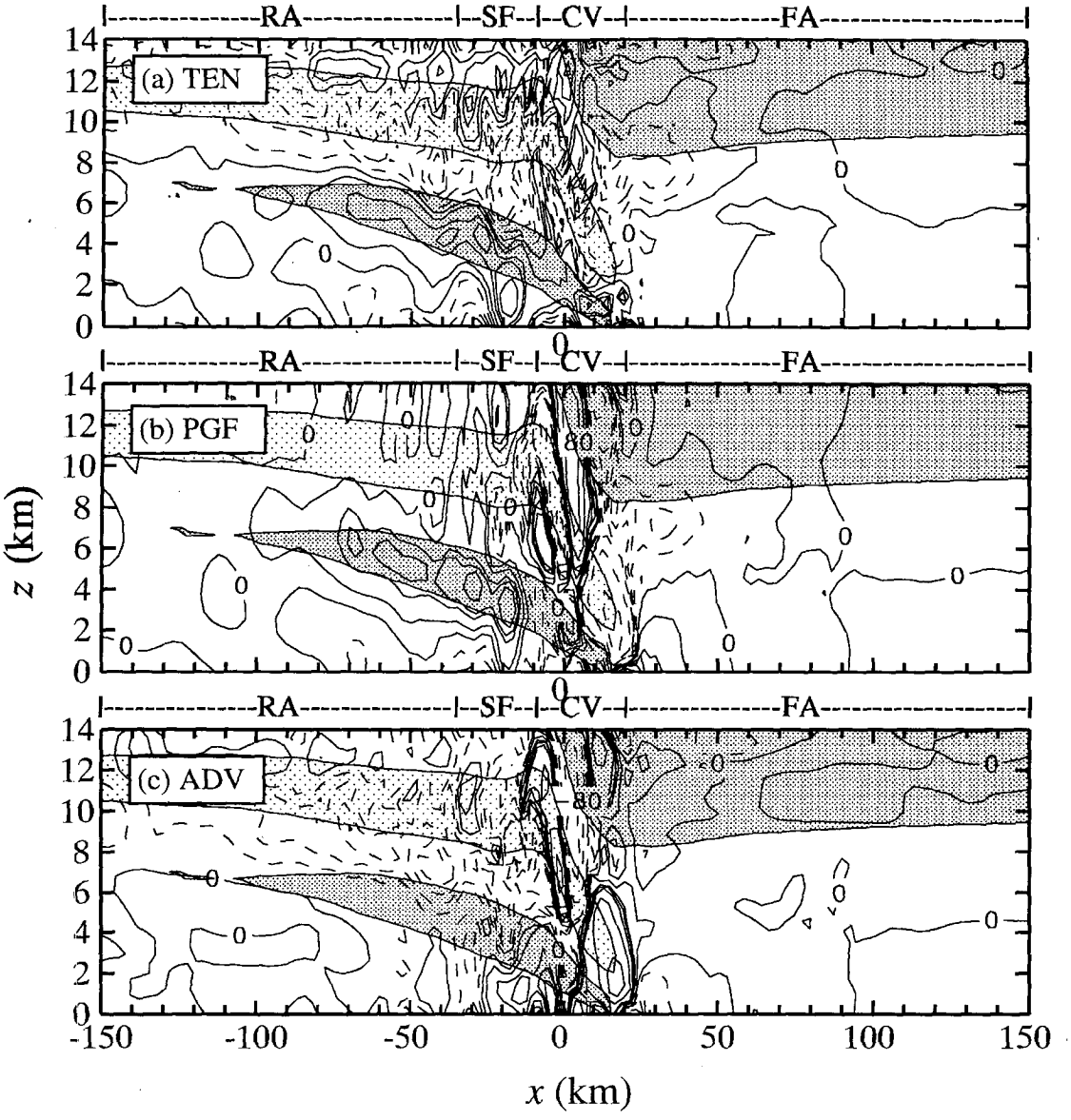

FIG. 7. One-hour-averaged fields of (a) TEN, (b) PGF, and (c) ADV in u-momentum equation (5) during the initial stage (t = 7.5–8.5 h) of the storm. Fields are contoured at −300, −240, −180, −120, −80, −40, −20, −15, −10, −5, 0, 5, 10, 15, 20, 40, 80, 120, 180, 240, and 300 m s^{-1} h^{-1}. Positive (RTF) tendency is in solid lines and negative (FTR) tendency is dashed. RTF flow greater than 3 m s^{-1} is heavily shaded, and FTR flow less than −18 m s^{-1} is lightly shaded. Regions of CV, SF, RA, and FA are shown in the bars above.

cending FTR flow by producing FTR flow change in middle to upper levels.

c. *Mature stage*

In the mature stage (t = 10–11 h), the simulated squall system was fully developed with pronounced mesoscale airflows (Figs. 1b and 2b). In the convective precipitation region (x = 20–50 km in Fig. 8a), the tendency field shows RTF increases at middle to upper levels and FTR increases at low to midlevels, although it is hard to see in the tight contour lines (shown more clearly in Fig. 10a). In the trailing-stratiform precipitation region (x = −90 to 20 km in Fig. 8a), the tendency shows a strong local RTF flow increase at upper levels, which results in a weakening of the diverging upper-level flow (see Fig. 1b), and a widespread FTR flow increase at midlevels, which implies the rearward extension and increased leaning back of the ascending FTR flow. At low levels, the net tendency in the stratiform precipitation region is to increase the RTF flow, inducing the downward

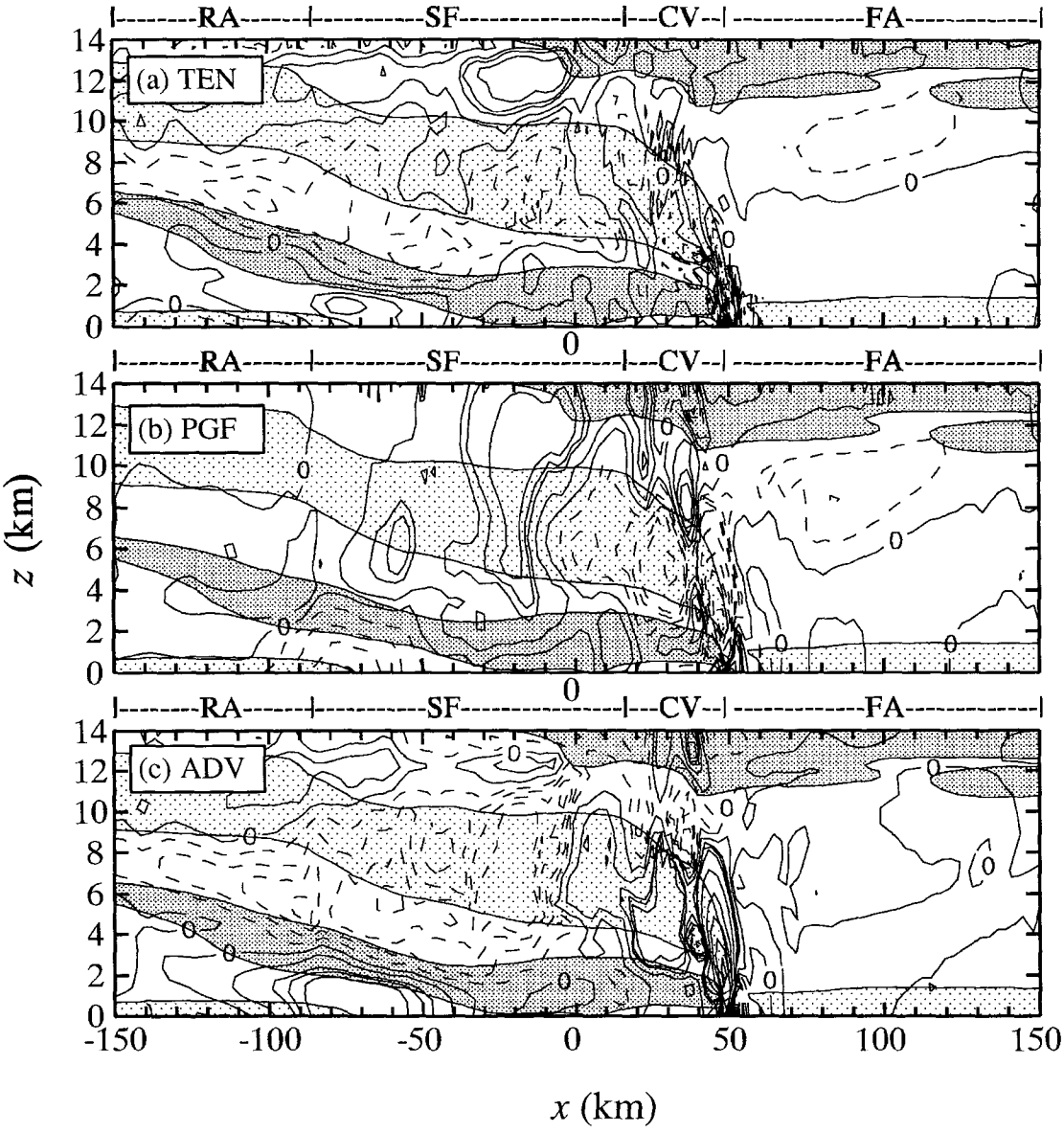

FIG. 8. Same as Fig. 7 except for terms in u-momentum equation (5) averaged in the mature stage (t = 10–11 h).

penetration of the descending rear inflow. Note that the acceleration–deceleration couplet (centered at x = −10 km, z = 7 km and x = −20 km, z = 12 km in Fig. 8a) corresponds to the intensifying mesoscale updraft (x = −25 km, z = 10 km in Fig. 2b).

Pressure-gradient force (in Fig. 8b) associated with the midlevel meso-γ-scale low strongly increases FTR flow in the convective precipitation region (x = 20 to 50 km) and the forward part of the stratiform precipitation region (x = −10 to 20 km), thus driving the ascending FTR flow and transporting hydrometeors rearward to form the trailing stratiform precipitation region. This intense FTR acceleration (peak value −333 m s^{-1} h^{-1}), determined by the cloud model simulation with 1-km horizontal resolution, is an order of magnitude greater than that produced by a mesoscale model simulation with 25-km horizontal resolution [−25 m s^{-1} h^{-1}; see Fig. 4b of Gao et al. (1990)], or that determined from the sounding data with 80-km horizontal resolution [−10 m s^{-1} h^{-1}; see Fig. 7a of Gallus and Johnson (1992)]. *The enhancement of the pressure-gradient force by a factor of 10–30 in the cloud model indicates that better-resolved convective-scale processes are necessary for the proper quantitative assessment of the generation and transport of momentum within the 10–11 June storm.*

Pressure-gradient force also produces RTF accelerations throughout most of the stratiform precipitation region ($x = -90$ to -10 km in Fig. 8b) to slow down the ascending FTR flow. A weak FTR acceleration is also found at low levels in the stratiform precipitation region ($x = -90$ to -60 km in Fig. 8b), which drives the low-level FTR flow beneath the intruding rear inflow. Qualitatively, the simulated pressure-gradient force in the convective precipitation region agrees well with those obtained by Gao et al. (1990, see their Fig. 4b) and Gallus and Johnson (1992, see their Fig. 7a). However, their pressure-gradient force in the stratiform precipitation region is mostly FTR, opposite to our result (mostly RTF). Their analysis across the stratiform precipitation region may have been affected by the large-scale pressure gradient [associated with a shortwave trough–ridge system aloft; see Figs. 2b and 4b of Gao et al. (1990)], which is not included in our cloud model simulation.

Total advection (Fig. 8c) shows a strong increase of RTF flow in the convective precipitation region ($x = 20$ to 50 km), opposing the intense FTR increase produced by pressure-gradient force. Behind the forward part of the stratiform precipitation region ($x < -10$ km), total advection produces an FTR flow increase in middle to upper levels, thus inducing the rearward extension and horizontal tilting of the ascending FTR flow. In low levels, the increase of RTF flow by total advection reflects the downward penetration of the descending rear inflow.

d. *Slowly decaying stage*

Because of the assumed constant convectively favorable condition in the prestorm environment, the simulated storm shows only a slow trend of weakening or decay in the late stage ($t = 12.5$–13.5 h). The overall distribution of the momentum generation and advection processes during the slowly decaying stage (Fig. 9) exhibits a more weakly organized but qualitatively similar structure to that in the mature stage (Fig. 8).

5. Area-average momentum budgets

In this paper, we consider the role of the squall line system in the large-scale budget of momentum. This problem is posed by considering a large horizontal area of which the squall system occupies a subregion. One may think of this area as the grid area of a general circulation model or as a region surrounded by an array of rawinsondes. Such a region may contain a population of clouds, of which a squall line with trailing stratiform precipitation region is one member. To represent the role of the cloud population in the mean conditions over such an area, the standard approach adopted in this study is to perform averaging over the region and let the cloud properties be represented as deviations from the averages of kinematic, thermodynamic, and microphysical variables. In our 2D framework, we let the fine-mesh domain play the role of the large-scale area. It is 300 km across and contains the squall system as well as surrounding anvil regions. This large-scale region contains a cloud population of only one member—the squall line with a trailing stratiform precipitation region.

Before inquiring into the role of the cloud system in terms of deviations from the mean flow, we examine the momentum equation averaged horizontally over the model domain. Let [ ] represent an area average over the 300-km-wide area A where the squall line is embedded. It is given by

$$[(\ \ )] \equiv \frac{1}{L}\int_0^L (\ \ )dx. \tag{7}$$

Let $\langle\ \ \rangle_i$ represent an average over a subregion i of the total domain A. Applying (7) to (5), we obtain

$$\left[\overline{\frac{\delta u_s}{\partial t}}\right] = \sum_i \left(-\sigma_i \left\langle \overline{c_p \theta_{v0} \frac{\partial \pi}{\partial x}} \right\rangle_i - \sigma_i \left\langle \overline{u_s \frac{\partial u_s}{\partial x}} \right\rangle_i - \sigma_i \left\langle \overline{w \frac{\partial u_s}{\partial z}} \right\rangle_i + \sigma_i \langle \overline{D_u} \rangle_i \right), \tag{8}$$

where the summation is over all the subregions represented in (1) (i represents the four regions FA, CV, SF, and RA). The factor σ_i is the fraction of the total domain A covered by subregion i.

The relative roles of the terms in (8) are qualitatively similar in each of the stages of the squall line's development. Therefore, for the remainder of this discussion, we examine only the large-scale budget in the mature stage.

Figure 10a shows the convective region contribution to the terms on the right-hand side of (8) for the mature stage ($t = 10$–11 h). The PGF produces a strong FTR (negative) tendency in the lower and middle levels ($0 < z < 8.5$ km) and weak RTF (positive) tendency in upper levels ($z > 8.5$ km). This pressure gradient force has a qualitatively similar profile to those of Gao et al. (1990, see their Fig. 9a) and Gallus and Johnson (1992, see their Fig. 15a), although their profiles remain negative above 320 mb (~8.5 km). HAD is roughly out of phase with VAD, consistent with Gao et al. (1990, see their Figs. 4a and 4c) and Caniaux et al. (1995, see their Fig. 21a). Subgrid-scale TRB is the smallest effect. *TEN is a small residual among other forcing terms,* and it is FTR (negative) in lower levels (below 4 km) and RTF (positive) at midlevels (4 km $< z <$ 8 km).

The area-weighted u-momentum terms in the stratiform precipitation region (Fig. 10b) have similar magnitudes to their convective counterparts (Fig. 10a); however, their vertical profiles are quite different. The PGF in the stratiform precipitation region generates

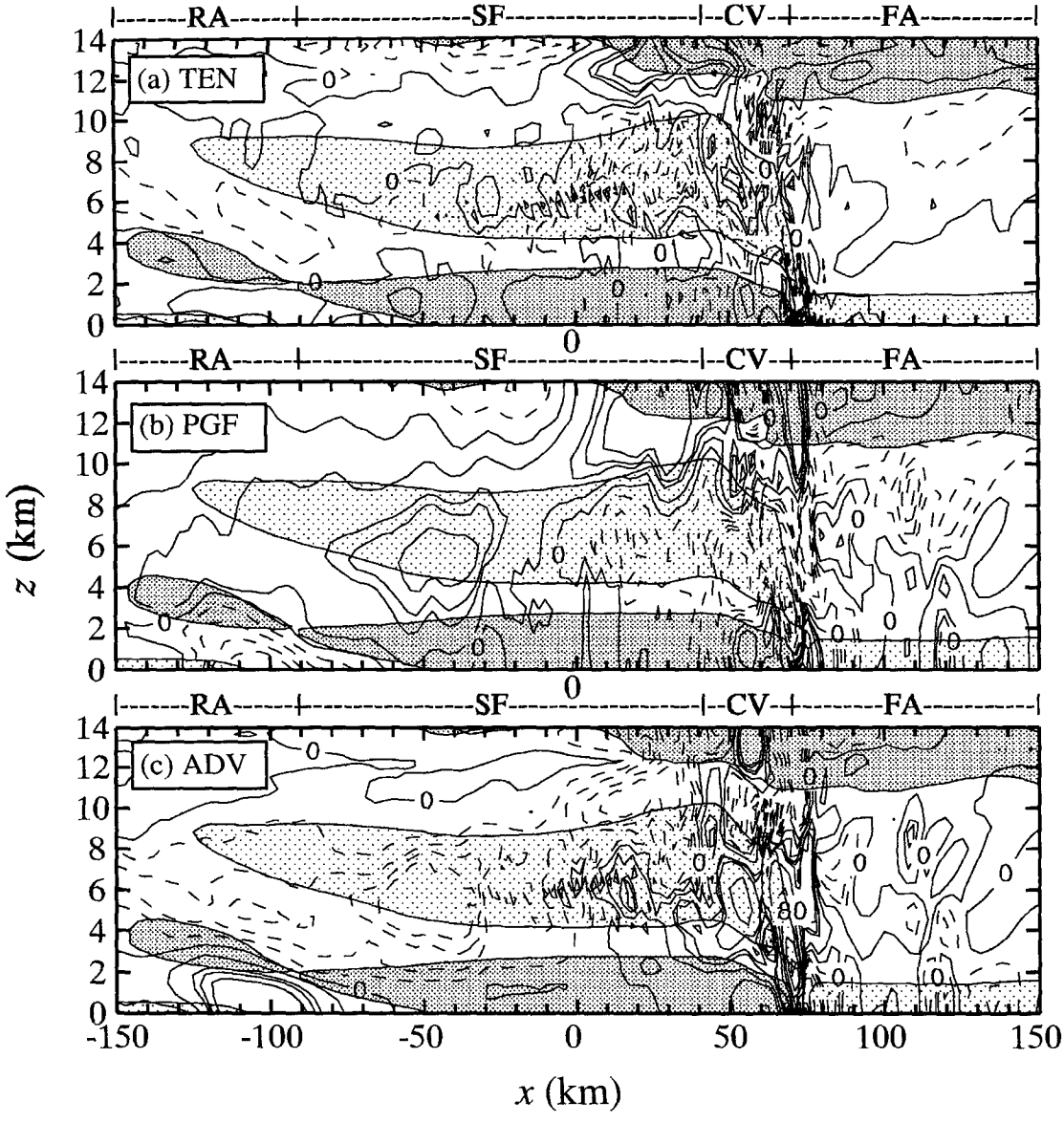

FIG. 9. Same as Fig. 7 except for terms in u-momentum equation (5) averaged in the slowly decaying stage (t = 12.5–13.5 h).

RTF tendency throughout the entire troposphere except at lower levels (below 2 km). HAD oscillates in the vertical and again is strongly out of phase with VAD. Subgrid-scale TRB is again the smallest term. TEN in the stratiform precipitation region dominates over that in all the other subregions; thus, *calculation of the correct momentum tendency in the stratiform precipitation region is essential to computing the overall effect of the storm on the large-scale momentum field.* The net tendency in the stratiform precipitation region is RTF (positive) in lower ($z < 2$ km) and upper levels ($z > 10$ km), and FTR (negative) in between (2 km $< z <$ 10 km), which is consistent with Gallus and Johnson (1992; see their Fig. 18a). This net tendency indicates the horizontal tilting of the ascending FTR flow and the downward penetration of the descending rear inflow in the stratiform precipitation region.

Figures 10c and 10d show the effects of the rear and forward anvil regions on the large-scale u-momentum tendency. Their effects on the large-scale tendency are generally less than those of the convective and stratiform precipitation regions. The curves in Figs. 10c,d generally show variations hovering around the zero-acceleration axis while the curves in Figs. 10a,b show much wider fluctuations. The contributions of TEN by the rear and forward anvil regions are not, however,

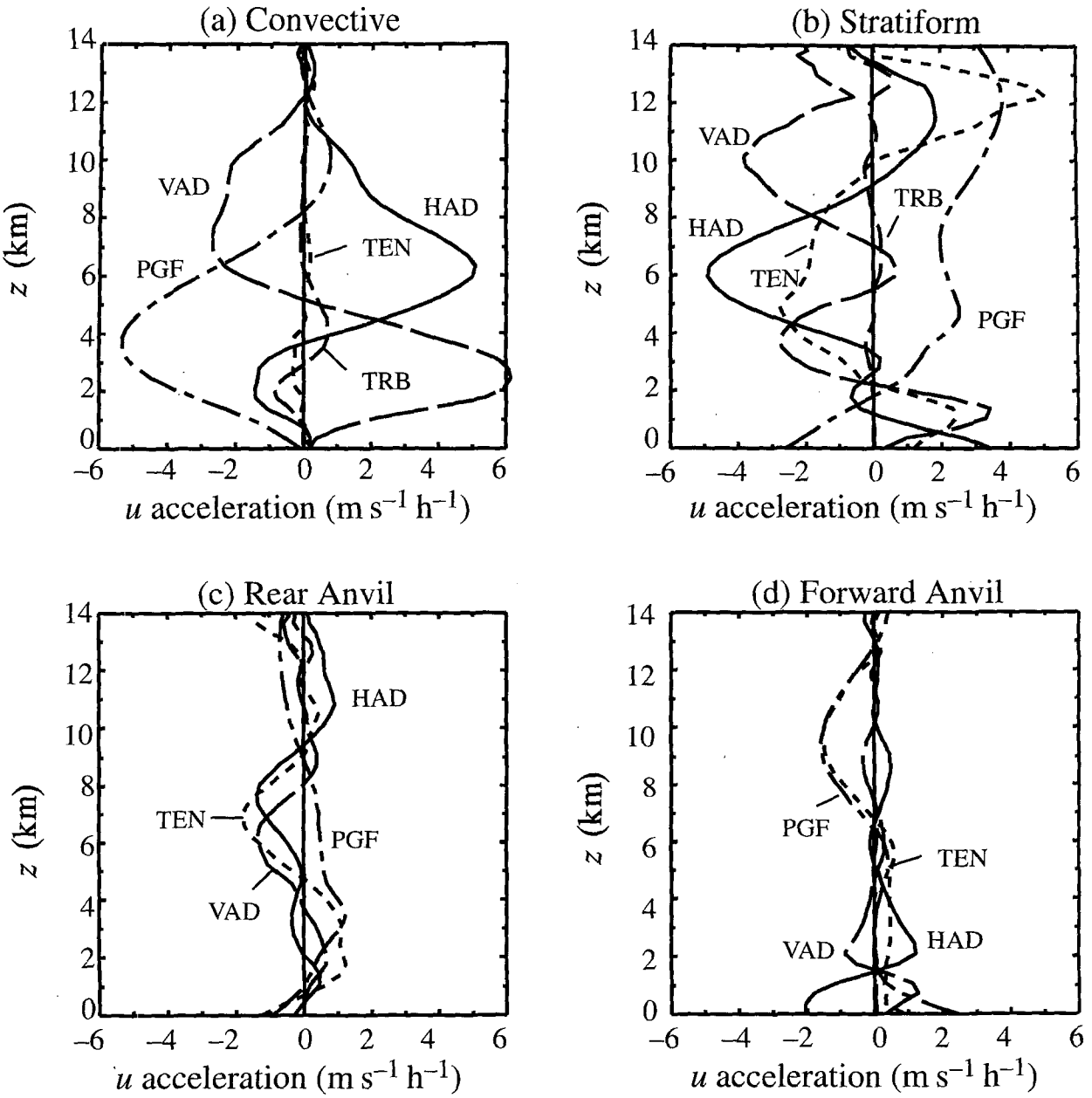

FIG. 10. Area-weighted TEN, HAD, VAD, PGF, and TRB in u-momentum equation (8) over the four subregions during the mature stage (t = 10–11 h). Positive tendency is RTF and negative tendency is FTR.

negligible compared to the net tendency in the stratiform precipitation region. TEN in the rear anvil region is positive at lower to middle levels (z = 1–5 km), while TEN in the stratiform precipitation region is positive at low levels (z < 2.5 km), indicating the acceleration of the sloping rear inflow.

Figure 11 shows the large-scale u-momentum budget. The curve labeled TEN is the left-hand side of (8). The curves labeled PGF, HAD, VAD, and TRB are the four terms on the right-hand side of (8), after they are summed over the four subregions of the domain. Figure 11 shows that, over the large-scale area A, PGF generates FTR tendency in low to midlevels (z < 6.5 km) and RTF tendency above (z > 6.5 km). VAD increases RTF flow in low levels (z < 4.5 km) and FTR flow above (z > 4.5 km). HAD produces an increase of RTF flow in upper levels (z > 8 km) and a weak increase of FTR flow in mid to lower levels (z < 8 km). TEN over the large-scale area A is RTF in lower (z < 3.5 km) and upper levels (z > 10.5 km),

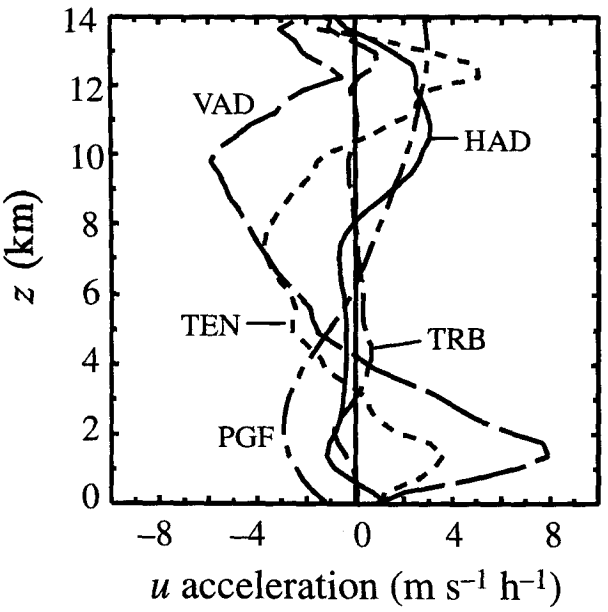

FIG. 11. Same as Fig. 10 except for terms in u-momentum equation (8) over the large-scale area A during the mature stage (t = 10–11 h).

and FTR in midlevels (3.5 km < z < 10.5 km). This vertical profile is similar to that of the stratiform precipitation region (TEN curve in Fig. 10b). The variation of TEN with time over the lifecycle of the squall system for the convective and stratiform precipitation regions is further shown in Fig. 12. It is clear from Fig. 12 that *once the system matures, the stratiform precipitation region determines the net momentum tendency of the large-scale area A.*

6. Impact of momentum flux on mean flow

We can rewrite the momentum equation in flux form by combining it with the mass-continuity equation. When we do this (in section 7), we obtain terms involving the fluxes by both the mean flow and eddy motion (deviations from the mean flow). The large-scale mean flow then changes according to the convergence of these fluxes in concert with pressure-gradient forces. LeMone and Moncrieff (1994) argue that one should try to avoid subdividing the flow into mean and perturbation quantities in computing the effect of the mesoscale system on the large-scale momentum field. They partition the flow, instead, by streamline pattern and obtain useful analytic representations of the total flow in the system. However, their approach assumes that the system is steady state and two-dimensional—conditions often not met in real cloud populations. So adopting their approach requires caution. The formulation in terms of mean flow and perturbations in this study is more general in that it makes no a priori assumption about storm structure or steadiness. Individual cloud systems do not have to be two-dimensional or steady state, and the large-scale area over which averages are taken may contain a variety of cloud types.

a. Formulation of momentum flux

We define means and perturbations of a velocity component V ($V = u$ or w) as

$$V = \bar{V} + V', \tag{9}$$

and

$$V = [V] + V^*, \tag{10}$$

where $\bar{V}$ in (9) is the time average defined by (6), and $[V]$ in (10) is the spatial average defined by (7). In (6) and (7), T = 1 h for each of the three lifecycle stages of the storm, and L = 300 km for the large-scale area A in which the storm is embedded. Following Priestly (1949) for the decomposition of large-scale heat fluxes in general circulations, we decompose the total vertical flux of storm-relative horizontal momentum $\rho_0[\overline{u_s w}]$ into three physically distinct parts:

$$\underset{T_{\text{tot}}}{\rho_0[\overline{u_s w}]} = \underset{S_m}{\rho_0[\bar{u}_s][\bar{w}]} + \underset{S_e}{\rho_0[\bar{u}_s^* \bar{w}^*]} + \underset{T_e}{\rho_0[\overline{u_s' w'}]}, \tag{11}$$

where ρ_0 is the basic-state density, $\rho_0[\bar{u}_s][\bar{w}]$ is the momentum transport by steady mean flow (S_m), $\rho_0[\bar{u}_s^* \bar{w}^*]$ is the transport by standing eddies (S_e), and $\rho_0[\overline{u_s' w'}]$ is the transport by transient eddies (T_e). The steady mean flow represents the mean flow across the 300-km large-scale area; standing eddies compose the steady-state mesoscale circulation, while the transient eddies are the temporally fluctuating convective-scale flow. The approximation in (11) assumes that terms of the forms $\overline{(\ )'(\ )'}$ and $[(\ )^*[(\ )^*]]$ are negligible. The model output verifies that this assumption is highly accurate in our case.

b. Weak transient eddies

Model output also verifies that over the large-scale domain of width L = 300 km the temporal fluctuations of u_s and w are only weakly correlated on the 1-h timescale. Figure 13, which shows the vertical profiles of each of the terms in (11), illustrates this result: the term T_e in (11) is much smaller than either S_m or S_e. Similar results were found by Caniaux et al. (1995) for a tropical West African squall line with a broad trailing stratiform precipitation region (see their Figs. 19 and 20). This result means that (11) becomes

$$T_{\text{tot}} \approx \rho_0[\overline{u_s w}] \approx S_m + S_e. \tag{11a}$$

The 1-h averaged velocity field in the simulated storm thus behaves *as if* the storm were in a steady state. This result indicates that on the 1-h timescale the steady-state two-dimensional idealization of Moncrieff (1992) applies to the simulated two-dimensional storm, even

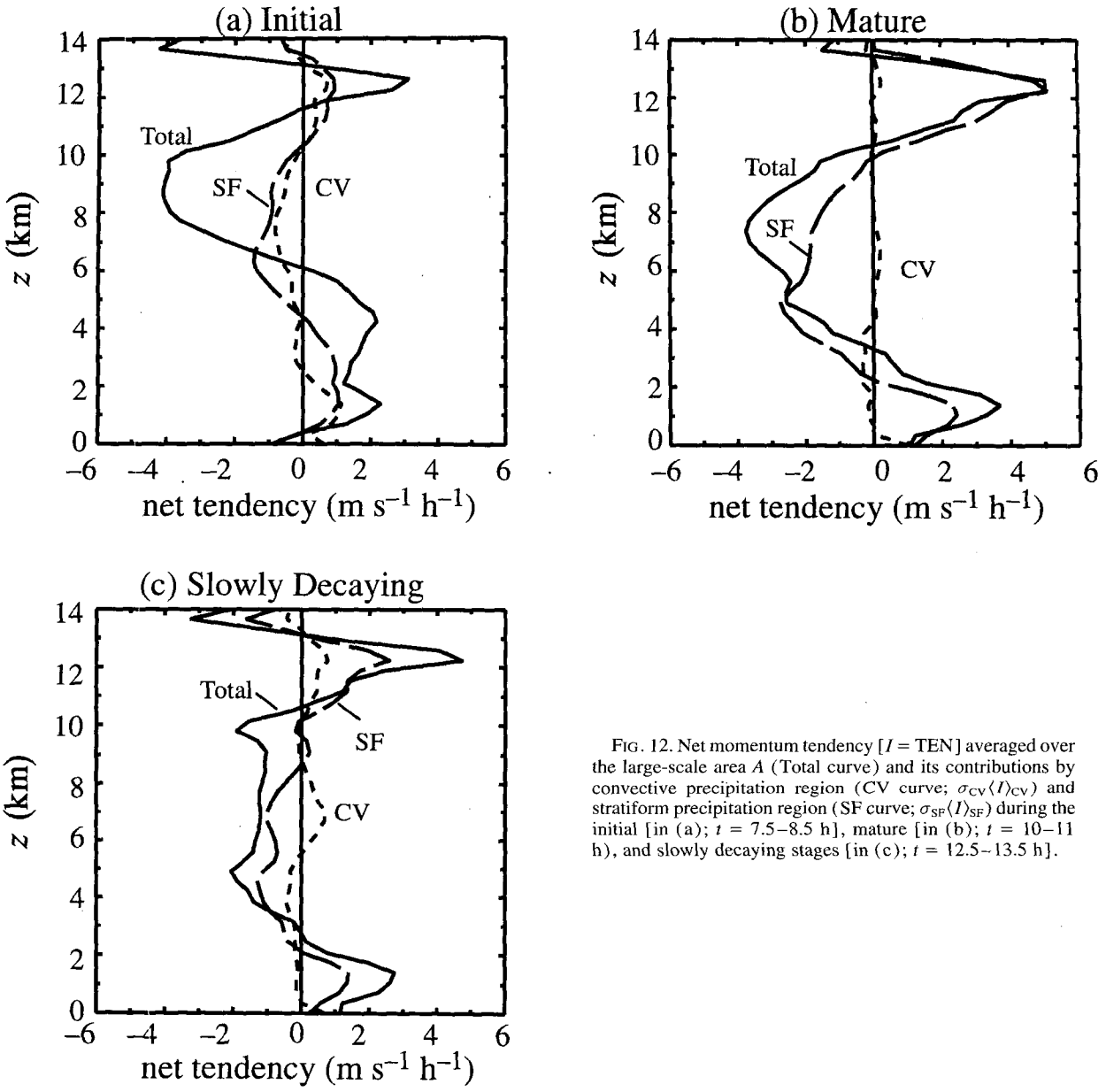

FIG. 12. Net momentum tendency [I = TEN] averaged over the large-scale area A (Total curve) and its contributions by convective precipitation region (CV curve; $\sigma_{CV}\langle I\rangle_{CV}$) and stratiform precipitation region (SF curve; $\sigma_{SF}\langle I\rangle_{SF}$) during the initial [in (a); t = 7.5–8.5 h], mature [in (b); t = 10–11 h), and slowly decaying stages [in (c); t = 12.5–13.5 h].

though we made no a priori assumption of steady-state conditions.

c. Negative momentum flux

It is shown in Fig. 13 that the total momentum flux T_{tot} is negative at all levels, and so are each of the components S_m, S_e, and T_e. All of the fluxes are transporting FTR momentum upward or RTF momentum downward. At upper levels ($z > 6.5$ km), most of the momentum is transported by steady mean flow (S_m curve). Figure 14 shows the wind vectors of domain-averaged mean flow ($[\overline{u_s}]$ and $[\overline{w}]$; Fig. 14a), standing eddy ($\overline{u_s}^*$ and $\overline{w}^*$; Fig. 14b), and total wind ($\overline{u_s}$ and $\overline{w}$; Fig. 14c) during the mature stage. Mean FTR flow combines with mean upward motion across the whole domain (Fig. 14a). The transport by standing eddies (curve S_e in Fig. 13) accounts for most of the total momentum transport at lower to middle levels ($z < 6.5$ km). The mesoscale circulation shows clearly in the standing-eddy wind field (Fig. 14b), in which the upward branch contains FTR flow, while the downward branch consists primarily of the sloping RTF flow.

d. Vertical convergence of momentum flux

Moncrieff (1992) and LeMone and Moncrieff (1994) work with the combined flux T_{tot}. They ide-

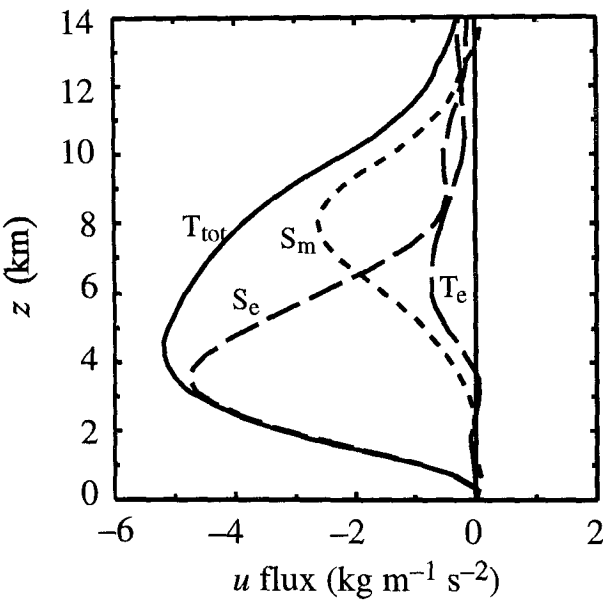

FIG. 13. Total vertical flux of storm-relative momentum (T_{tot}) and its three components—the transports by the steady mean flow (S_m), standing eddies (S_e), and transient eddies (T_e) in (11)—over the large-scale area A during the mature stage (t = 10–11 h).

alize the combined mean and eddy flow (Fig. 14c) in terms of three flow branches (rear overturning current, jump updraft, and overturning updraft). Using these three flow branches, Moncrieff (1992) shows that the vertical convergence of the momentum flux is given by

$$-\frac{1}{\rho_0}\frac{\partial}{\partial z}(\rho_0\langle\overline{u_s}\overline{w}\rangle) = \frac{1}{L_m}\left(\overline{u_s}^2 + \frac{\overline{p_m}}{\rho_0}\right)\Bigg|_0^{L_m}, \quad (12)$$

where

$$\langle(\ )\rangle = \frac{1}{L_m}\int_0^{L_m}(\ )dx. \quad (12a)$$

Here, L_m is the dynamical scale of the mesoscale convective system, and p_m is the pressure in the mesoscale convective system. Equation (12) states that the vertical convergence of the total momentum flux at a given altitude must be accounted for by the net change of kinetic energy plus enthalpy (per unit mass) across the system—if the system is indeed two-dimensional and steady state.

Let us assume that the dynamical scale of the system L_m is, in our case, identical to the fine-mesh domain width L. Then the averaging operators defined in (7) and (12a) are identical (i.e., $\langle(\ )\rangle = [(\ )]$), and it follows from (11) and (11a) that

$$\rho_0\langle\overline{u_s}\overline{w}\rangle \approx T_{tot} \approx S_m + S_e. \quad (12b)$$

Substituting (12b) in (12) gives

$$-\frac{1}{\rho_0}\frac{\partial}{\partial z}T_{tot} \approx -\frac{1}{\rho_0}\frac{\partial}{\partial z}(S_m + S_e)$$
$$\approx \frac{1}{L_m}\left(\overline{u_s}^2 + \frac{\overline{p_m}}{\rho_0}\right)\Bigg|_0^{L_m}. \quad (12c)$$

As a further test of whether our 1-h-average model calculations are consistent with Moncrieff's (1992) steady-state theory, we calculate the left and right sides of (12c) from model outputs and see if we obtain the same result. The left-hand side of (12c) is plotted in Fig. 15a and the right-hand side in Fig. 15b, for three stages of squall line development. The two sets of curves are virtually identical. Thus, the vertical convergence of total momentum flux for the time-averaged numerical simulation results could be represented in terms of the change of kinetic energy plus enthalpy across the system, as advocated by Moncrieff (1992) and LeMone and Moncrieff (1994).

The idealization of Moncrieff (1992) seems to fit the present simulation very well. However, when the calculations are filtered to a 1-h timescale, it may not fit so well under slightly more general temporal or spatial conditions. At a smaller timescale, T_e becomes larger, and the idealization cannot be applied. Also, the simulation in this study is verified against the data for only the *portion* of the 10–11 June squall line that exhibited the most ideal two-dimensional structure within the larger system (Biggerstaff and Houze 1993). In portions of the storm better described by three-dimensional dynamics (Skamarock et al. 1994), the momentum budget may have different characteristics, and the two-dimensional idealization should be used with appropriate caveats and caution.

e. *Splitting the momentum flux convergence into mean and eddy components*

In view of the above consistency checks, we could accurately represent the vertical convergence of total momentum flux for the 1-h-averaged numerical model results in terms of the kinetic energy plus enthalpy change across the system. For our purpose, however, it is more useful to consider the flux convergence on the left-hand side of (12c) and decompose it into mean and eddy components [Eq. (11) and Figs. 14a,b]. The reason is that our goal differs from that of Moncrieff (1992) and LeMone and Moncrieff (1994). They seek insight into the overall dynamics of a storm in which forces are in balance, while we seek insight into the subtle *imbalance* producing large-scale momentum tendency and, in particular, how the storm's internal structure may affect those imbalances. Since it is *only* the eddy flux that varies across the storm (Fig. 14b), it is useful to isolate the contribution of the eddy flux convergence ($-\rho_0^{-1}\partial S_e/\partial z$) to the total flux convergence and determine whether it has different behaviors

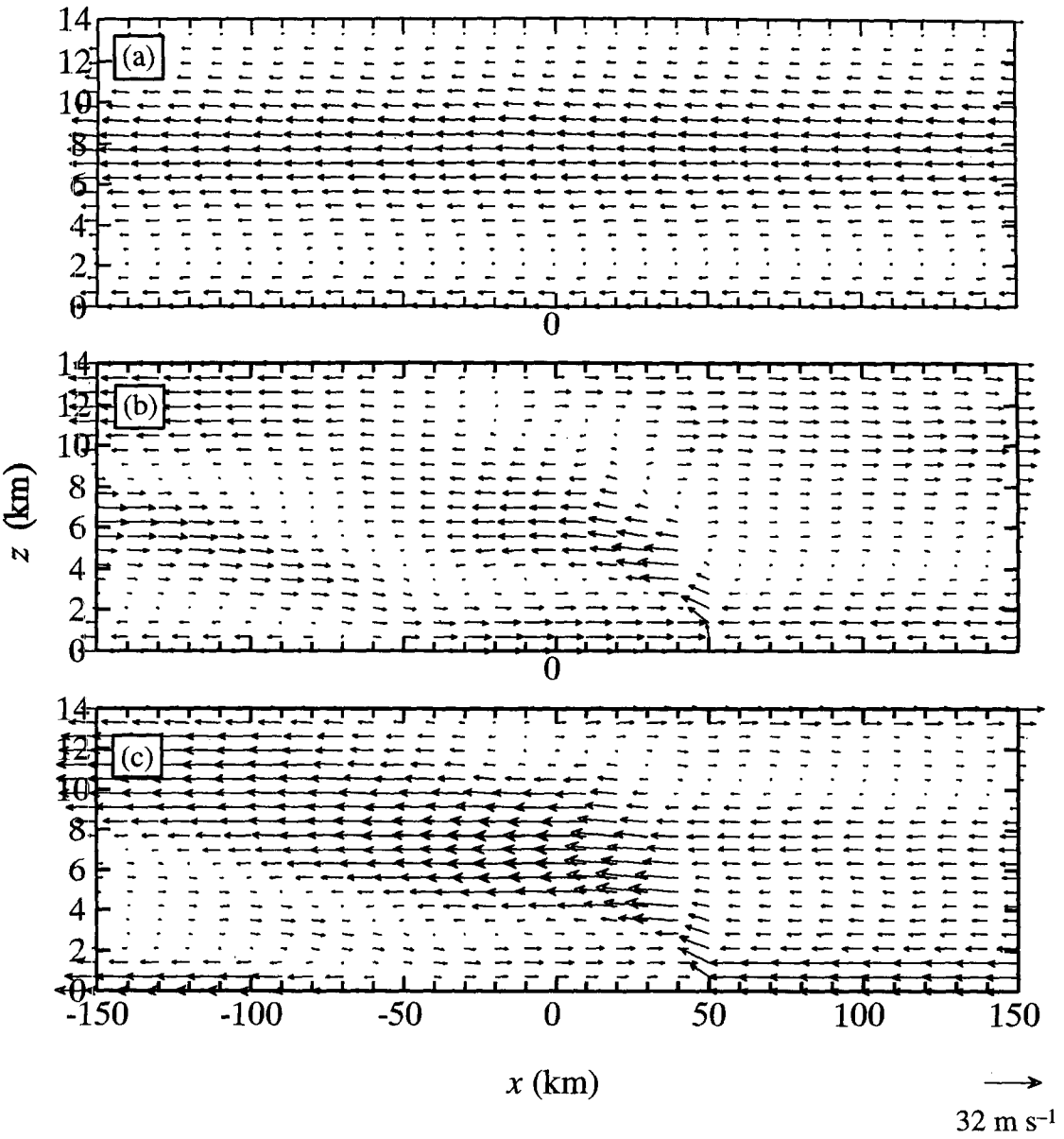

FIG. 14. Vertical cross section of vectors of (a) domain-averaged wind ($[\overline{u_s}]$, $[\overline{w}]$), (b) standing eddy ($\overline{u_s}^*$, $\overline{w}^*$), and (c) total wind ($\overline{u_s}$, $\overline{w}$) during the mature stage (t = 10–11 h) of the storm.

in the convective and stratiform precipitation areas and other subregions of the storm.

f. Contributions of storm subregions to eddy momentum flux

Figure 16 shows the vertical momentum flux by standing eddies S_e during the 1-h period at the mature stage of the storm. The largest values are confined mainly to the convective precipitation region and mainly to the low to midlevels (below 6.5 km). Figure 17 further shows the contribution of each subregion to the total standing-eddy momentum flux in the mature stage of the storm. The stratiform precipitation region (SF curve), forward anvil (FA curve), and rear anvil (RA curve) contribute only weakly to the standing-eddy momentum flux. The convective precipitation region (CV curve) contributes 65%–75% of the total standing-eddy momentum flux (Total curve). Sounding data from the 10–11 June storm also indicated negative momentum fluxes over the convective precipitation region and the entire squall system (Gallus and Johnson 1992, see their Fig. 19). Normalized by areal fraction, their fluxes were weaker than ours (especially

for the convective region flux, which was weaker than ours by a factor of 4–10). Evidently, the sounding data cannot fully resolve the detailed convective-scale processes.

7. Large-scale momentum budget

a. *Formulation of time- and area-averaged momentum budget*

We now consider the momentum budget of large-scale area A by rewriting the time-averaged u-momentum equation (5) in flux form. Combining Eq. (5) with the anelastic mass continuity equation ($\nabla \cdot \rho_0 \mathbf{v} = 0$, where $\mathbf{v}$ is the two-dimensional wind vector) and applying the horizontal averaging operator (7) over the fine-mesh domain length L, we obtain

$$\left[\overline{\frac{\delta u_s}{\partial t}}\right] = -\left[\frac{\partial}{\partial x}(\overline{u_s}^2)\right] - \frac{1}{\rho_0}\frac{\partial}{\partial z}(\rho_0[\overline{u_s w}]) - \left[\overline{c_p \theta_{v0} \frac{\partial \pi}{\partial x}}\right] + [\overline{D_u}]. \quad (13)$$

Neglecting the turbulence term $[\overline{D_u}]$, ignoring the transient eddy term T_e in Eq. (11), and substituting Eq. (11) into Eq. (13) leads to the time- and space-averaged momentum equation

$$\underset{\text{TEN}}{\left[\overline{\frac{\delta u_s}{\partial t}}\right]} \approx \underset{\text{PGF}}{-\left[\overline{c_p \theta_{v0} \frac{\partial \pi}{\partial x}}\right]} \underset{\text{HMF}}{-\left[\frac{\partial}{\partial x}(\overline{u_s}^2)\right]} \underset{\text{VMF}}{-\frac{1}{\rho_0}\frac{\partial}{\partial z} S_m} \underset{\text{VEF}}{-\frac{1}{\rho_0}\frac{\partial}{\partial z} S_e}. \quad (14)$$

The term on the left of (14) is net momentum tendency (TEN), and terms on the right of (14) are the horizontal PGF, horizontal mean-flow flux convergence (HMF), vertical mean-flow flux convergence (VMF), and vertical eddy-flux convergence by standing eddies (VEF), respectively. Note from (12c) that the last two terms in (14) combine to form Moncrieff's (1992) total flux convergence, which may be expressed in terms of the kinetic energy and enthalpy difference across the system—in the special conditions that apply in this case.

We will see below that the primary terms determining the large-scale momentum tendency TEN are the pressure gradient force PGF and the combined effects of the vertical flux convergence (VMF + VEF). We will also see that over the system *as a whole* PGF and (VMF + VEF) tend to oppose each other. Indeed, in a steady-state system of the type idealized by Moncrieff (1992), these two effects exactly balance over the system as a whole (in the absence of horizontal flux convergence). In an evolving large-scale momentum field, it is the slight *imbalance* between these two effects that determines how the momentum field changes.

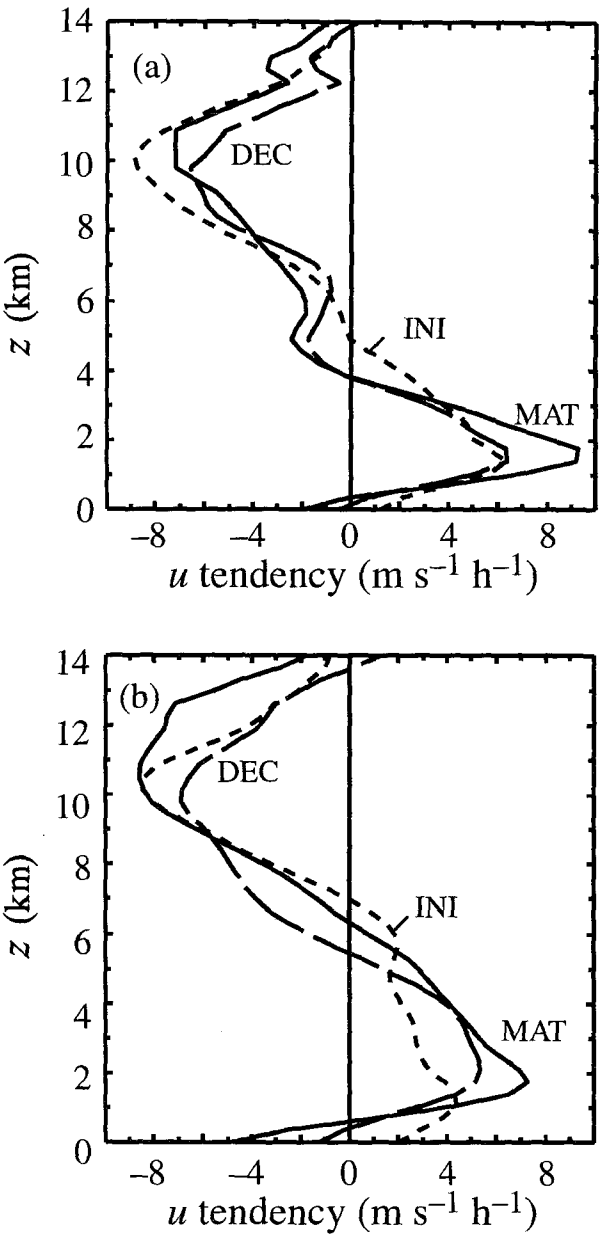

FIG. 15. (a) Left- and (b) right-hand sides of Eq. (12) for the initial (INI; t = 7.5–8.5 h), mature (MAT; t = 10–11 h), and slowly decaying (DEC; t = 12.5–13.5 h) stages of the storm.

In (14), the only terms that can vary from one subregion of the storm to another are the PGF and the VEF. In the next two subsections, we will examine how these two terms vary from one subregion to the next.

b. *Pressure-gradient force*

First consider the large-scale momentum change produced by the PGF in (14) during the mature stage

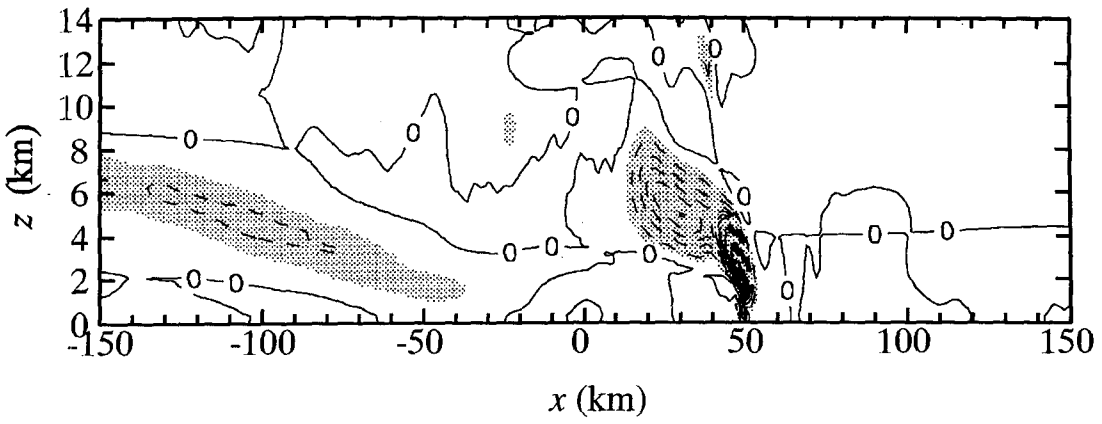

FIG. 16. Vertical cross section of standing-eddy velocity product ($\overline{u_s} \times \overline{w}$) during the mature stage (t = 10–11 h) of the storm. Contour interval is 10 m^2 s^{-2} and shaded area is for velocity product less than −5 m^2 s^{-2}.

(t = 10–11 h). Figure 18 displays the large-scale time- and area-averaged pressure-gradient force and its area-weighted subregional contributions, which show that PGF varies strongly as a function of location within the squall system. In the convective precipitation region (CV curve), the pressure-gradient force results in FTR tendency in the lower and middle levels (z < 8 km) and weak RTF tendency aloft (z > 8 km). However, pressure-gradient force in the stratiform precipitation region (SF curve) produces a weak FTR tendency in the lower level (z < 2 km) and moderate RTF tendency throughout the middle and upper levels (z > 2 km). Over the anvil regions (RA and FA curves), the tendency induced by pressure-gradient force is much weaker than that in the precipitation regions (CV and SF curves). Therefore, over the large-scale area A (Total curve), the convective precipitation region contributes most of the FTR pressure-gradient tendency at the lower and midlevels (z < 6.5 km), and the stratiform precipitation region contributes most of RTF pressure-gradient tendency at mid to upper levels (z > 6.5 km).

c. *Vertical convergence of eddy flux*

Figure 19 shows the VEF [(14)] and its area-weighted subregional contributions. This figure clearly indicates the dominance of the convective region contribution (CV curve) to the eddy-flux convergence over

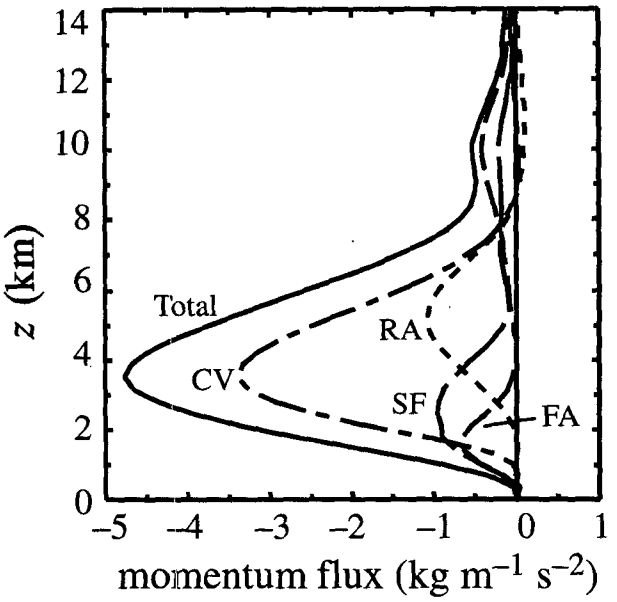

FIG. 17. Same as Fig. 5 except for the momentum flux by standing eddies [S_e in (11)] during the mature stage (t = 10–11 h).

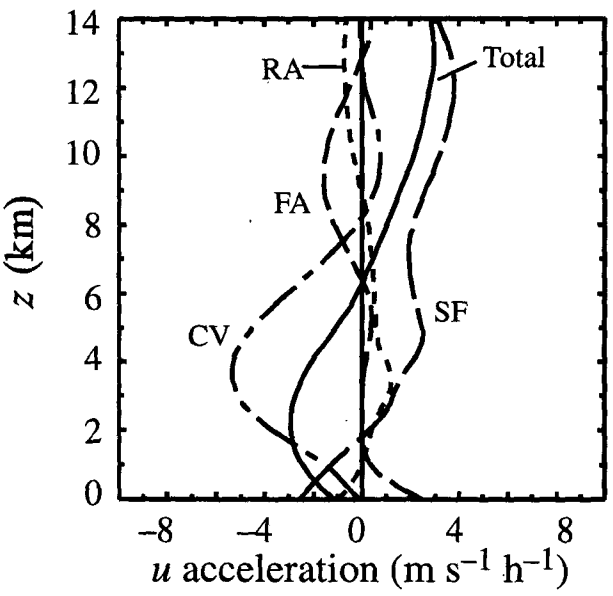

FIG. 18. Same as Fig. 5 except for PGF (14) during the mature stage (t = 10–11 h).

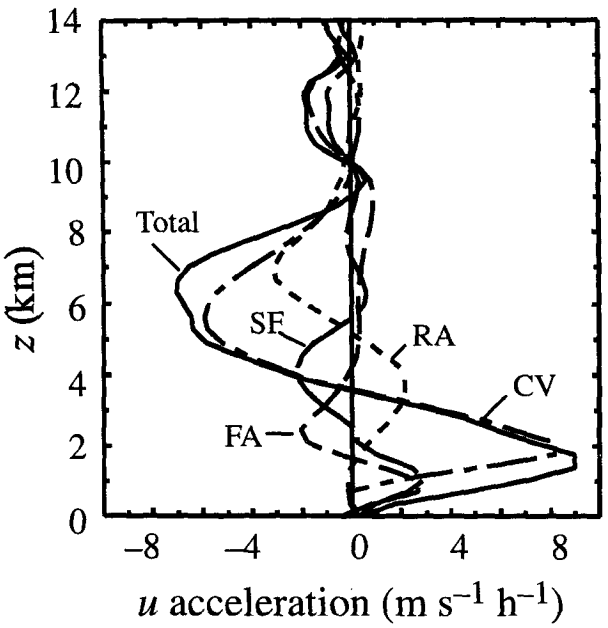

FIG. 19. Same as Fig. 5 except for VEF in (14) during the mature stage (t = 10–11 h).

the large-scale area A (Total curve). In the convective precipitation region, standing-eddy flux convergence strongly contributes to RTF flow at low levels ($z < 3.5$ km) and FTR flow at midlevels ($3.5 < z < 9$ km). Standing-eddy flux convergence in the stratiform precipitation region (SF curve) produces much weaker (by a factor of 3–4) momentum changes than in the convective precipitation region. The effect of stratiform-region eddy-flux convergence on the large-scale mean flow is to lower the midlevel (low level) peak of FTR (RTF) increase produced by the convective precipitation region. The convergence of eddy flux associated with the descending rear inflow (near z = 7 km) in the rear anvil region (RA curve) results in an increase of RTF flow below ($z < 7$ km) and FTR flow aloft ($z > 7$ km). The eddy flux in the forward anvil region (FA curve) creates momentum changes at much lower levels (FA curve maximum at z = 1.5 km in Fig. 17), thus producing momentum change at lower levels (RTF increases for $z < 2$ km and FTR increases for 2 km $< z < 4$ km).

d. Total large-scale momentum tendency

Figure 20 shows the net momentum tendency over the large-scale area A and its different physical contributions [terms in (14)]. The vertical flux convergence by mean flow (VMF) and standing eddies (VEF) contribute large portions of the large-scale TEN in (14). These curves are consistent with those in Fig. 11, which shows the same TEN as in Fig. 20 but subdivided according to the terms in the advective form of the momentum equation (8) instead of the flux form (14). VMF and VEF in (14) derive primarily from the VAD in (8), which according to Fig. 11 is the dominant term in the advective form of the momentum equation. HMF largely comes from the horizontal advection HAD in (8), and the vertical profile of HAD in Fig. 11 is similar to the profile of HMF in Fig. 20.

The flux form of the momentum budget (Fig. 20) shows that the vertical eddy-flux convergence (VEF) is much stronger than any of the other terms at low and middle levels. It largely determines the sense of the overall tendency TEN, which is RTF at low levels ($z < 3$ km) and FTR at midlevels ($3 < z < 10$ km). The PGF and HMF together account for the large-scale momentum tendency in upper levels ($z > 10.5$ km).

8. Conclusions

Since our model simulation excludes the large-scale horizontal variation of the environment, the calculated momentum generation and transport are produced by the squall line alone (i.e., not by large-scale forcing). The simulation is two-dimensional, and it calibrates reasonably well against data from the two-dimensional segment of the 10–11 June 1985 squall line with trailing stratiform precipitation region observed in PRE-STORM. The very high spatial and temporal resolution (Δx = 1 km, Δt = 6 s) of the cloud model provides detailed insight into the convective-scale processes within the system. These small-scale processes are essential in the momentum balance and transport. One

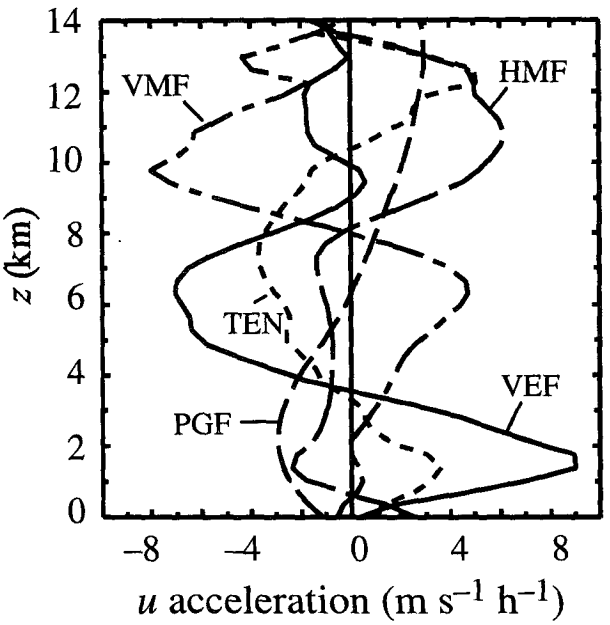

FIG. 20. Momentum tendencies of large-scale area A by terms in (14)—HMF, VMF, PGF, VEF, and TEN—during the mature stage (t = 10–11 h).

caveat of this simulation is that the Coriolis effect is not included, so the readers may interpret the model results with some caution.

When the momentum equation is written in flux form, by combining it with the continuity equation and averaging over a large-scale area of horizontal width of 300 km and a time period of 1 h, we obtain terms involving the fluxes by the mean flow and eddy motion. Decomposition of total momentum flux into three physically distinct modes—transports by steady mean flow, standing eddies, and transient eddies—shows that in the middle to upper levels, the transport by steady mean flow contributes most of the total momentum flux. The transport by standing eddies explains most of the total momentum flux in low to middle levels. Transport by transient eddies is negligible. The dominance of momentum transport by two-dimensional steady-state circulation (mean flow plus standing eddies) shows that the 1-h averaged model simulation, and by inference the two-dimensional north-central segment of the 10–11 June squall line system itself, conform to Moncrieff's (1992) analytic idealization of a two-dimensional steady-state squall line. To what extent this idealization may be extended to the whole mesoscale convective system [as modeled by Skamarock et al. (1994)] or to the broader population of mesoscale convective systems [as described by Houze et al. (1990)] remains to be determined.

Figure 21 summarizes the momentum balance over a 300-km-wide large-scale area containing the simulated squall line system. The region is partitioned into four horizontal regions (convective precipitation area, stratiform precipitation area, rear and forward anvil regions) and into three broad altitude layers. In the lowest layer (0–4 km) and upper levels (10–14 km), the net momentum tendency (shown in Fig. 21b) is positive (increasing RTF flow), while at midlevels (4–10 km), the net tendency is negative (increasing FTR flow).

The arrows in Fig. 21a show how much each of the processes represented by the terms on the right-hand side of (14) contributes to the net momentum tendency in Fig. 21b, according to altitude and subregion of the storm. The strongest contributions are from the convective and stratiform precipitation zones. The arrows show, however, that *no* single process or any one subregion of the storm dominates the net momentum tendency over the large-scale area. The contribution from the convective precipitation region dominates at low levels, both convective and stratiform precipitation regions contribute significantly to net momentum tendency at midlevels, and the contribution from the stratiform precipitation region is essential at upper levels.

Figure 21a clearly illustrates that the net momentum tendency over the large-scale area is the result of competing processes; *the net momentum tendencies are a delicate imbalance of strong terms of opposite sign.* In particular, the following are noted:

- At low levels (0–4 km), the convective precipitation region alone determines the net momentum tendency on the large scale. The net RTF tendency (Fig. 21b) is the result of a competition of two strong but

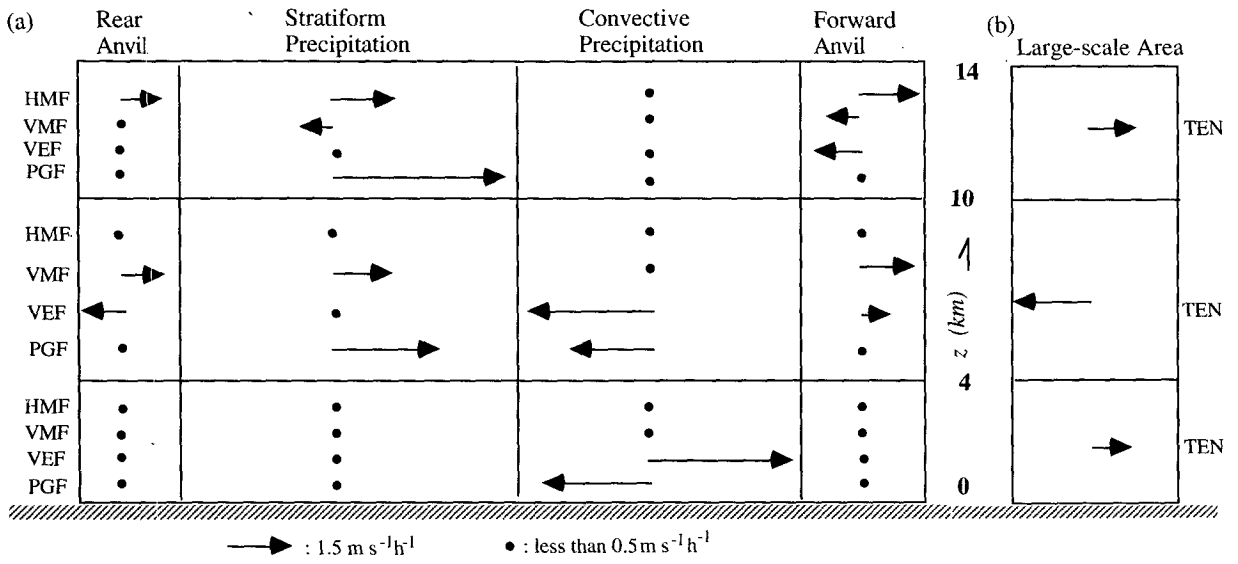

FIG. 21. (a) A block diagram showing the balance of area-weighted momentum-budget terms in (14) over four subregions of a large-scale area during the mature stage of the simulated 10–11 June 1985 squall line. Rightward-pointing arrow is for positive (rear to front) u-tendency and leftward-pointing arrow is for negative (front to rear) u-tendency. The length of arrow is proportional to the layer-averaged tendency produced by each budget term. A dot is for tendency less than 0.5 m s^{-1} h^{-1}. (b) as (a) except for net momentum tendency, the term on the left-hand side of (14), over the total 300-km-wide large-scale area.

oppositely directed processes in the convective precipitation region (Fig. 21a). The forward-directed tendency by the standing-eddy flux convergence, which in accordance with its sloping structure (Fig. 14b) transports low-level (midlevel) FTR (RTF) momentum upward (downward) in the convective updrafts (downdrafts), slightly outweighs the rearward-directed pressure-gradient tendency produced by the meso-γ-scale low under the sloping updrafts (Fig. 4b).

- At midlevels (4–10 km), all four subregions contribute significantly to the net tendency (Fig. 21b); the largest forces, however, occur in the convective and stratiform precipitation regions. The net tendency at midlevels (Fig. 21b) is FTR. The pressure-gradient tendencies (FTR in the convective region and RTF in the stratiform region) are both quite strong. In this case, they tend to cancel each other out so that the pressure-gradient acceleration contributes very little to the total tendency at midlevels. However, if the stratiform region were less well developed and the convective region were still strong, the pressure-gradient acceleration in that region might be weaker, leading to a net forward acceleration. Another strong process at midlevels is the vertical eddy-flux convergence in the convective region, which contributes a strong net FTR tendency; the eddy-flux convergence combines with the pressure gradient acceleration in the convective region to overwhelm the RTF pressure-gradient acceleration in the stratiform region, yielding the net FTR tendency in the midlevels (Fig. 21b). Vertical flux by the mean flow is not negligible at these levels, and the forward and rear anvils also make minor but not negligible contributions to the net tendency.
- At upper levels (10–14 km), the convective region (Fig. 21a) contributes very little to the overall momentum tendency (Fig. 21b). The dominant process is the RTF tendency in the stratiform region produced by the mesohigh aloft centered at 12 km (Fig. 4b).

These results show that computations of the large-scale momentum tendency produced by a squall line with a trailing-stratiform precipitation region are a strong function of the internal structure of the storm. Figure 21a conveys that the locus of the most active processes (as measured by the general length of the arrows) slopes rearward from low levels in the convective precipitation region to the upper levels in the stratiform precipitation region. These arrows show that all the terms in (14) are significant, and all of the subregions (horizontal and vertical) of the storm contribute rather differently to the net momentum tendency. The contributions by vertical standing-eddies flux convergence and by pressure-gradient forces attain the largest magnitudes; however, they tend to work in opposite directions, so that the resulting net momentum tendency is a small residual between these large terms, which behave differently from one region of the storm to another. It seems clear that storm structure can influence the nature of the net momentum tendency on the large scale; a storm dominated by a strong convective precipitation region could well produce a very different net large-scale momentum tendency than a storm with strong stratiform precipitation region and a weak convective precipitation region. Techniques to distinguish convective and stratiform precipitation regions from radar data (e.g., Steiner et al. 1995) may prove useful in this respect.

Thus, there appear to be no short cuts to the parameterization of momentum tendencies produced by mesoscale convective systems. Except for transient eddies, which do not produce a strong effect, all the processes of momentum generation and flux are important, and their relative importance varies with altitude and, importantly, from one subregion of the storm to the next. While this complexity presents a significant and daunting challenge for parameterizing momentum tendencies by squall lines in large-scale prediction and climate models, the well-defined and repeatable structure of squall lines with trailing stratiform precipitation (e.g., Houze et al. 1990) of the storm increases the tractability of the problem.

Acknowledgments. Professor R. G. Fovell guided the early modeling of the storm. Scott Braun, David Kingsmill, Peggy LeMone, Tom Matejka, Sandra Yuter, and an anonymous reviewer provided very helpful comments and suggestions. G. C. Gudmundson edited the manuscript and Kay Dewar drafted several of the figures. The calculation was performed at the National Center for Atmospheric Research, which is sponsored by the National Science Foundation. This research was supported by NSF Grant ATM-9409988.

REFERENCES

Augustine, J. A., and E. J. Zipser, 1987: The use of wind profilers in a mesoscale experiment. *Bull. Amer. Meteor. Soc.*, **68,** 4–17.

Biggerstaff, M. I., and R. A. Houze Jr., 1991a: Kinematic and precipitation structure of the 10–11 June 1985 squall line. *Mon. Wea. Rev.*, **119,** 3034–3065.

——, and ——, 1991b: Midlevel vorticity structure of the 10–11 June 1985 squall line. *Mon. Wea. Rev.*, **119,** 3066–3079.

——, and ——, 1993: Kinematics and microphysics of the transition zone of the 10–11 June 1985 squall line. *J. Atmos. Sci.*, **50,** 3091–3110.

Braun, S. A., and R. A. Houze Jr., 1994a: The transition zone and secondary maximum of radar reflectivity behind a midlatitude squall line: Results retrieved from Doppler radar data. *J. Atmos. Sci.*, **51,** 2733–2755.

——, and ——, 1994b: The heat and potential vorticity budgets of a midlatitude squall line. Preprints, *Sixth Conf. on Mesoscale Processes,* Portland, OR, Amer. Meteor. Soc., 335–338.

——, and ——, 1995a: Diagnosis of hydrometeor profiles from area-mean vertical velocity data. *Quart. J. Roy. Meteor. Soc.*, **121,** 23–53.

——, and ——, 1995b: Melting and freezing within a midlatitude mesoscale convective system. *Quart. J. Roy. Meteor. Soc.*, **121,** 55–77.

Caniaux, G., J.-P. Lafore, and J.-L. Redelsperger, 1995: A numerical study of the stratiform region of a fast-moving squall line. Part II: Relationship between mass, pressure, and momentum fields. *J. Atmos. Sci.*, **52,** 331–352.

Churchill, D. D., and R. A. Houze Jr., 1984: Development and structure of winter monsoon cloud clusters on 10 December 1978. *J. Atmos. Sci.*, **41,** 933–960.

Cunning, J. B., 1986: The Oklahoma–Kansas Preliminary Regional Experiment for STORM-Central. *Bull. Amer. Meteor. Soc.*, **67,** 1478–1486.

Fovell, R. G., and Y. Ogura, 1988: Numerical simulation of a midlatitude squall line in two dimensions. *J. Atmos. Sci.*, **45,** 3846–3879.

Gallus, W. A., Jr., and R. H. Johnson, 1991: Heat and moisture budget of an intense midlatitude squall line. *J. Atmos. Sci.*, **48,** 122–146.

——, and ——, 1992: The momentum budget of an intense midlatitude squall line. *J. Atmos. Sci.*, **49,** 422–450.

Gao, K., D.-L. Zhang, M. W. Moncrieff, and H.-R. Cho, 1990: Mesoscale momentum budget in a midlatitude squall line: A numerical case study. *Mon. Wea. Rev.*, **118,** 1011–1028.

Houze, R. A., Jr., 1982: Cloud clusters and large-scale vertical motions in the tropics. *J. Meteor. Soc. Japan,* **60,** 396–410.

——, 1989: Observed structure of mesoscale convective systems and implications for large-scale heating. *Quart. J. Roy. Meteor. Soc.*, **115,** 425–461.

——, 1993: *Cloud Dynamics.* Academic Press, 573 pp.

——, B. F. Smull, and P. Dodge, 1990: Mesoscale organization of springtime rainstorms in Oklahoma. *Mon. Wea. Rev.*, **118,** 613–654.

Johnson, R. H., and P. J. Hamilton, 1988: The relationship of surface pressure features to the precipitation and the air-flow structure of an intense midlatitude squall line. *Mon. Wea. Rev.*, **116,** 1444–1472.

Klemp, J. B., and R. B. Wilhelmson, 1978: The simulation of three-dimensional convective storm dynamics. *J. Atmos. Sci.*, **35,** 1070–1096.

LeMone, M. A., 1983: Momentum flux by a line of cumulonimbus. *J. Atmos. Sci.*, **40,** 1815–1834.

——, and M. W. Moncrieff, 1994: Momentum and mass transport by convective bands: Comparisons of highly idealized dynamical models to observations. *J. Atmos. Sci.*, **51,** 281–305.

——, G. M. Barnes, and E. J. Zipser, 1984: Momentum flux by lines of cumulonimbus over tropic oceans. *J. Atmos. Sci.*, **41,** 1914–1932.

Mapes, B. E., 1993: Gregarious tropical convection. *J. Atmos. Sci.*, **50,** 2026–2037.

——, and R. A. Houze Jr., 1995: Diabatic divergence profiles in western Pacific mesoscale convective systems. *J. Atmos. Sci.*, **52,** 1807–1828.

Moncrieff, M. W., 1981: A theory of organized steady convection and its transport properties. *Quart. J. Roy. Meteor. Soc.*, **107,** 29–50.

——, 1992: Organised mesoscale convective systems: archetypal dynamical models, mass and momentum flux theory, and parameterization. *Quart. J. Roy. Meteor. Soc.*, **118,** 819–850.

Orlanski, I., 1975: A rational subdivision of scales for atmospheric processes. *Bull. Amer. Meteor. Soc.*, **56,** 527–530.

Priestly, C. H. B., 1949: Heat transport and zonal stress between latitudes. *Quart. J. Roy. Meteor. Soc.*, **75,** 28–40.

Rutledge, S. A., R. A. Houze Jr., M. I. Biggerstaff, and T. Matejka, 1988: The Oklahoma–Kansas mesoscale convective system of 10–11 June 1985: Precipitation structure and single-Doppler radar analysis. *Mon. Wea. Rev.*, **116,** 1409–1430.

Schneider, E. K., and R. S. Lindzen, 1976: A discussion of the parameterization of momentum exchange by cumulus convection. *J. Geophys. Res.*, **81,** 3158–3161.

Skamarock, W. C., M. L. Weisman, and J. B. Klemp, 1994: Three-dimensional evolution of simulated long-lived squall lines. *J. Atmos. Sci.*, **51,** 2563–2584.

Smull, B. F., and R. A. Houze Jr., 1987: Rear inflow in squall lines with trailing stratiform precipitation. *Mon. Wea. Rev.*, **115,** 2869–2889.

Steiner, M., R. A. Houze Jr., and S. E. Yuter, 1995: Climatological characterization of three-dimensional storm structure from operational radar and rain gauge data. *J. Appl. Meteor.*, **34,** 1978–2007.

Stevens, D. E., R. S. Lindzen, and L. J. Shapiro, 1977: A new model of tropical waves incorporating momentum mixing by cumulus convection. *Dyn. Atmos. Oceans.*, **1,** 365–425.

Szeto, K. K., and H.-R. Cho, 1994: A numerical investigation of squall lines. Part II: The mechanics of evolution. *J. Atmos. Sci.*, **51,** 425–433.

Wilhelmson, R. B., and C.-S. Chen, 1982: A simulation of the development of successive cells along a cold outflow boundary. *J. Atmos. Sci.*, **39,** 1466–1483.

Yang, M.-J., and R. A. Houze Jr., 1995a: Multicell squall line structure as a manifestation of vertically trapped gravity waves. *Mon. Wea. Rev.*, **123,** 641–661.

——, and ——, 1995b: Sensitivity of squall-line rear inflow to ice microphysics and environmental humidity. *Mon. Wea. Rev.*, **123,** 3175–3193.

Zhang, D.-L., and K. Gao, 1989: Numerical simulation of an intense squall line during 10–11 June 1985 PRE-STORM. Part II: Rear inflow, surface wake lows and stratiform precipitation. *Mon. Wea. Rev.*, **117,** 2067–2094.

——, ——, and D. B. Parsons, 1989: Numerical simulation of an intense squall line during 10–11 June 1985 PRE-STORM. Part I: Model verification. *Mon. Wea. Rev.*, **117,** 960–994.

Zipser, E. J., 1977: Mesoscale and convective-scale downdrafts as distinct components of squall-line circulation. *Mon. Wea. Rev.*, **105,** 1568–1589.